Article

Cell Metabolism

# Cold exposure protects from neuroinflammation through immunologic reprogramming

## Graphical abstract

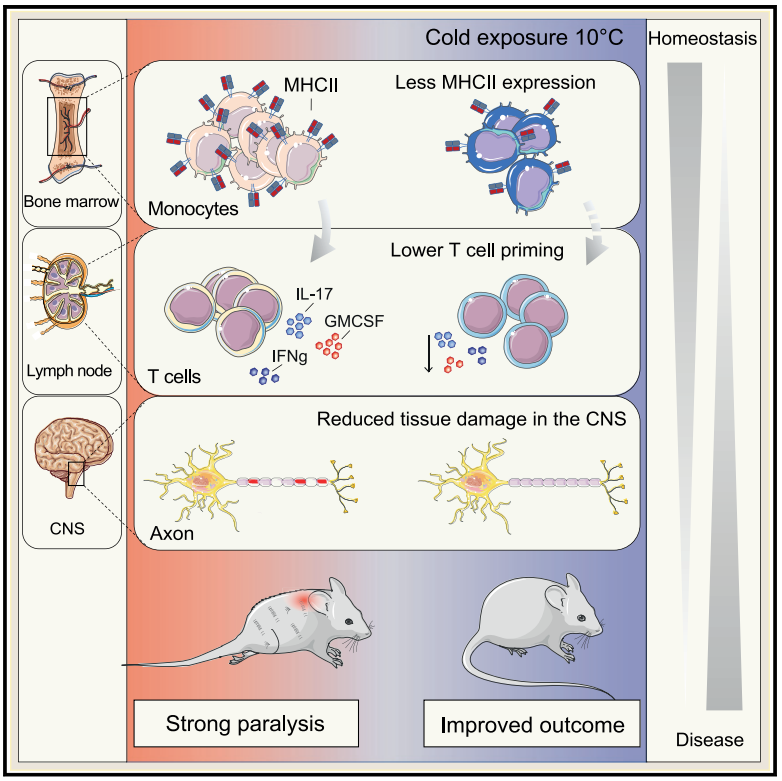


## Highlights

- Cold temperature modulates immunologic and metabolic phenotype of monocytes
- Cold promotes energetic trade-off between metabolic adaptations and autoimmunity in mice
- Cold exposure lowers MHCII on monocytes and ameliorates neuroinflammation
- Reduced T cell priming by monocytes is critical for the cold-induced EAE attenuation

## Authors

Martina Spiljar, Karin Steinbach, Dorothée Rigo, ..., Melanie Greter, Doron Merkler, Mirko Trajkovski

## Correspondence

doron.merkler@unige.ch (D.M.), mirko.trajkovski@unige.ch (M.T.)

## In brief

Spiljar et al. show that colder temperatures provoke an energetic trade-off between autoimmunity and thermogenesis in mice. Cold decreases MHCII on monocytes at steady state and in various inflammatory conditions including in a mouse model of multiple sclerosis. Further, cold suppresses autoreactive T cell priming and pathogenicity through the modulation of monocytes, thereby ameliorating neuroinflammation.

Spiljar et al., 2021, Cell Metabolism *33*, 2231–2246
November 2, 2021 
https://doi.org/10.1016/j.cmet.2021.10.002

CellPress

Cell Metabolism

CellPress
OPEN ACCESS

Article

# Cold exposure protects from neuroinflammation through immunologic reprogramming

Martina Spiljar,[1,2,9] Karin Steinbach,[3] Dorothée Rigo,[1,2] Nicolas Suárez-Zamorano,[1,2] Ingrid Wagner,[3] Noushin Hadadi,[1,2] Ilena Vincenti,[3] Nicolas Page,[3] Bogna Klimek,[3] Mary-Aude Rochat,[1,2] Mario Kreutzfeldt,[3] Claire Chevalier,[1,2] Ozren Stojanović,[1,2] Olivia Bejuy,[4] Didier Colin,[5] Matthias Mack,[6] Dilay Cansever,[7] Melanie Greter,[7] Doron Merkler,[3,8,10,*] and Mirko Trajkovski[1,2,10,11,*]

[1]Department of Cell Physiology and Metabolism, Faculty of Medicine, Centre Médical Universitaire (CMU), University of Geneva, Geneva, Switzerland
[2]Diabetes Center, Faculty of Medicine, University of Geneva, Geneva, Switzerland
[3]Department of Pathology and Immunology, Faculty of Medicine, Centre Médical Universitaire (CMU), University of Geneva, Geneva, Switzerland
[4]CIBM Centre for BioMedical Imaging, Faculty of Medicine, University of Geneva, 1211 Geneva, Switzerland
[5]Small Animal Preclinical Imaging Platform, Faculty of Medicine, University of Geneva, 1211 Geneva, Switzerland
[6]Department of Internal Medicine II - Nephrology, University Hospital Regensburg, Regensburg, Germany
[7]Institute of Experimental Immunology, University of Zurich, Zurich, Switzerland
[8]Division of Clinical Pathology, Geneva University Hospitals, Geneva, Switzerland
[9]Present address: Evergrande Center for Immunologic Diseases, Harvard Medical School and Brigham and Women's Hospital, Boston, MA, USA
[10]These authors contributed equally
[11]Lead contact
*Correspondence: doron.merkler@unige.ch (D.M.), mirko.trajkovski@unige.ch (M.T.)
https://doi.org/10.1016/j.cmet.2021.10.002

## SUMMARY

Autoimmunity is energetically costly, but the impact of a metabolically active state on immunity and immune-mediated diseases is unclear. Ly6C$^{hi}$ monocytes are key effectors in CNS autoimmunity with an elusive role in priming naive autoreactive T cells. Here, we provide unbiased analysis of the immune changes in various compartments during cold exposure and show that this energetically costly stimulus markedly ameliorates active experimental autoimmune encephalomyelitis (EAE). Cold exposure decreases MHCII on monocytes at steady state and in various inflammatory mouse models and suppresses T cell priming and pathogenicity through the modulation of monocytes. Genetic or antibody-mediated monocyte depletion or adoptive transfer of Th1- or Th17-polarized cells for EAE abolishes the cold-induced effects on T cells or EAE, respectively. These findings provide a mechanistic link between environmental temperature and neuroinflammation and suggest competition between cold-induced metabolic adaptations and autoimmunity as energetic trade-off beneficial for the immune-mediated diseases.

## INTRODUCTION

Maintaining immunity requires substantial metabolic resources (Buck et al., 2017; Demas and Nelson, 2012; Ganeshan et al., 2019; Hotamisligil, 2017; McDade, 2005; O'Neill et al., 2016) for steady-state systemic immune surveillance and during inflammation, leading to the generation of millions of immune cells daily. The life history theory (Stearns, 1992) proposes that prioritization of resources between biological programs would depend on the environment. In hostile environments, resources are shifted away from growth and reproduction programs into maintenance programs (Okin and Medzhitov, 2012; Stearns, 1992; Wang et al., 2019). In addition to immunity, these maintenance traits include adaptations to energy scarcity and also adaptations to changes in the environmental temperature. Exposure to cold provokes a high-cost, high-gain physiologic response aimed at reducing heat dissipation (e.g., by vasoconstriction) and increasing heat production, mainly by activating the brown adipose tissue (BAT) and browning of the subcutaneous adipose tissue (SAT). BAT catabolizes energy to enable generation of heat, a function conferred by the uncoupling protein 1 (UCP1). The cold-induced BAT activation is triggered by sympathetic innervation (Cannon and Nedergaard, 2004; Stojanović et al., 2018). Norepinephrine released from the nerve endings stimulates the beta 3-adrenergic receptor, and agonists of this receptor are frequently used to mimic cold exposure and experimentally induce thermogenesis.

In autoimmunity, the organism develops an energetically costly pro-inflammatory immune response (Okin and Medzhitov, 2012). Such high-energy-demanding processes may compete

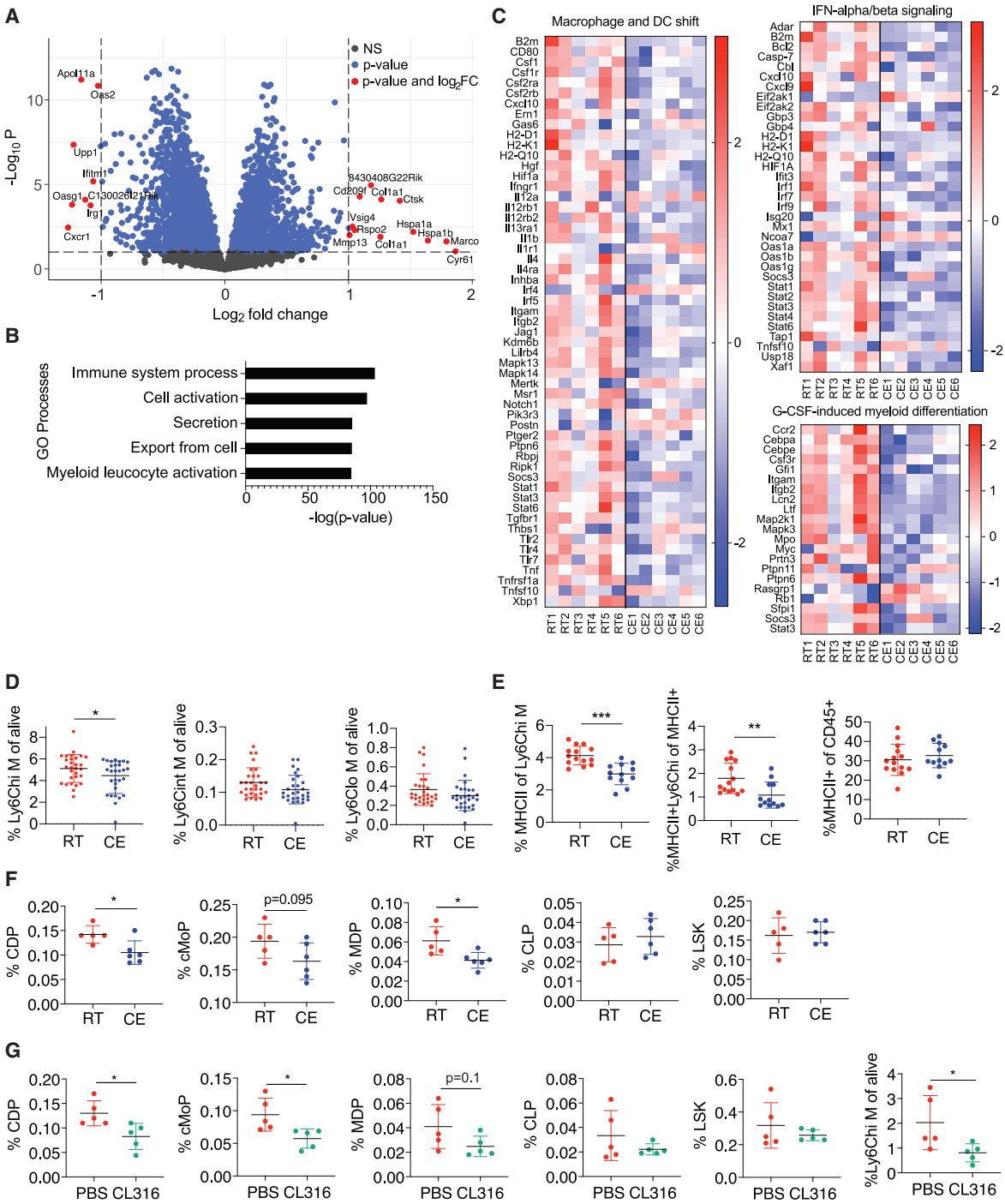


**Figure 1. Cold exposure impacts monocytes in the bone marrow**

(A) Volcano plot showing the up- and downregulated transcripts by RNA sequencing in the bone marrow of cold-exposed mice for 2 weeks at 10°C compared to room temperature counterparts (n = 6 mice per group).

(B) MetaCore Gene Ontology processes analysis displaying the top 5 enriched processes of mice as in (A).

(C) Shown are 3 of 4 heatmaps that were regulated in the same direction (>80% of genes in the same direction) from the top 10 differentially regulated MetaCore Pathway Maps of mice as in (A). Full pathway names are "Macrophage and dendritic cell phenotype shift in cancer," "Immune response_IFN-aplha/beta signaling via JAK/STAT" and "G-CSF induced myeloid differentiation."

(B and C) The cutoff on differentially regulated genes considered for the pathway analysis is $p < 0.05$ and pathways are considered deregulated with $p < 0.05$. Shown are –log(p value).(D) Flow cytometry analysis of bone marrow cells of mice as in (A). Percentage of Ly6C high (hi), intermediate (int), and low (lo) monocytes of total, single $CD45^+$ alive cells.

*(legend continued on next page)*

with each other, and prioritization of one task over the other may be a result of an energetic trade-off. This concept can be of particular interest for autoimmunity, in which introducing an additional energy-costly program may result in a milder immune response and disease outcome. In contrast to the well-described immune status during obesity (Grant and Dixit, 2015; Hotamisligil, 2017; Kohlgruber et al., 2016; Li et al., 2020; Man et al., 2017), the repercussions of a metabolically active phenotype on autoimmunity and the potential systemic effects on the immune-mediated diseases are unknown.

Experimental autoimmune encephalomyelitis (EAE) is an animal model for multiple sclerosis (MS), the most frequent autoimmune demyelinating disease of the central nervous system (CNS). Similar to MS, EAE is exacerbated by a high caloric diet and obesity (Hasan et al., 2016; Piccio et al., 2008; Timmermans et al., 2014; Winer et al., 2009), notably characterized by a positive energy balance. $CD4^+$ T cells and monocytes are important cellular players in the pathogenesis of EAE. Among $CD4^+$ T cells, distinct encephalitogenic subsets are essentially involved in disease precipitation and are characterized by certain cytokine signatures, including interleukin17 (IL-17), granulocyte-macrophage colony stimulating factor (GM-CSF), and interferon gamma (IFNg). Monocytes and monocyte-derived cells are crucial for the resulting tissue destruction of the CNS, particularly during the effector phase of EAE (Ajami et al., 2011; Fife et al., 2000; Izikson et al., 2000; King et al., 2009; Mildner et al., 2009; Serbina and Pamer, 2006). Thereby, these monocytes and monocyte-derived cells can express pro-inflammatory inducible nitric oxide synthase (INOS) (m1-like) or anti-inflammatory arginase 1 (ARG1) (m2-like) and, in addition, can exert antigen-presenting function via major histocompatibility complex class II (MHCII) upregulation. The role of monocytes in priming the autoreactive T cells in CNS autoimmunity, and whether cold exposure could affect this interaction, remains unclear.

Our study provides an unbiased characterization of the immune system in different compartments in healthy conditions and during CNS autoimmunity following exposure to lower environmental temperature. We demonstrate that cold exposure renders monocytes less activated in the bone marrow, in the circulation, and in the CNS. The change in the monocyte phenotype affects priming of pathogenic T cells during neuroinflammation, resulting in reduced T cell cytokine expression and, consequently, attenuated EAE. Our data suggest a competition between the thermogenic response to cold exposure and autoimmunity leading to a constrained immune response, which could be of therapeutic importance in neuroinflammation and potentially other autoimmune-mediated or infectious diseases.

## RESULTS

### Cold exposure modulates myeloid cells in bone marrow at steady state

To explore the impact of cold exposure on the immune system, we first focused on the bone marrow where immune cells originate from. We performed RNA sequencing of the bone marrow from mice exposed to 10°C for 2 weeks following an acclimatization period and compared them to mice kept at room temperature (Figures 1A and S1A). We shortlisted the significantly different genes ($p < 0.05$) for pathway and gene ontology analyses and considered pathways and terms significantly deregulated or enriched when $p < 0.05$. Among the 5,088 enriched terms identified by MetaCore Gene Ontology processes, "Myeloid Leukocyte Activation" was among the top five most enriched terms (Figure 1B). MetaCore Metabolic Network analysis identified 41 enriched networks (Figure S1B), whereas MetaCore Pathway Maps revealed 885 pathways that were changed. Among the top ten most significantly regulated ones (Figure S1C), four pathways were consistently changed (>80% of genes in same direction) (Figures 1C and S1D). These were macrophage and dendritic cell (DC) shift, granulocyte-macrophage colony stimulating factor (G-CSF)-induced myeloid differentiation, IFN-alpha/beta signaling, and transcription regulation-granulocyte development, which mainly contain genes important for myeloid cell activation and differentiation.

We then examined the impact of cold exposure at cellular and protein level within the bone marrow by flow cytometry. While cold exposure did not affect the number of total bone marrow cells (Figure S1E), there was a decrease in $Ly6C^{hi}$, but not $Ly6C^{int}$ or $Ly6C^{lo}$, monocytes (Figure 1D). $Ly6C^{hi}$ monocytes showed phenotypical changes characterized by reduced MHCII expression (Figure 1E), a marker for antigen presentation and activation. Within the total $MHCII^+$ cells, the population of $MHCII^{+-}$ $Ly6C^{hi}$ monocytes was decreased, while the percentage of total $MHCII^+$ cells within the bone marrow remained unchanged (Figure 1E; gating strategy in Figure S1F). The differences in the MHCII expression on protein level were consistent with the observations from RNA sequencing, where MHCII genes were within the top downregulated pathways (Figure 1C).

To address whether cold exposure decreases the monocytes by affecting hematopoiesis, we analyzed hematopoietic progenitors in the bone marrow similarly as previously described (Hettinger et al., 2013; Luo et al., 2015; Merad et al., 2013). In three

(E) Percentage of $MHCII^+$ cells of $Ly6C^{hi}$ monocytes (left), $MHCII^+$ $Ly6C^{hi}$ monocytes of total $MHCII^+$ cells (middle), and total $MHCII^+$ cells of $CD45^+$ cells (right) of mice as in (A), as determined by flow cytometry.

(F) Bone marrow immune cell progenitors of mice as in (A) were analyzed by flow cytometry and percentage of total alive single CD45+ cells is shown for common dendritic cell progenitors (CDPs), common monocyte progenitors (cMoPs), monocyte-dendritic cell progenitors (MDPs), common lymphoid progenitors (CLPs), and $Lin^-$ $Sca1^+$ $c\text{-}KIT^+$ cells (LSKs), as determined by flow cytometry.

(G) Immune cell progenitor flow cytometry analysis of mice that were intraperitoneally (i.p.) injected with beta 3 adrenoreceptor agonist CL316,243 (CL316) or vector (PBS) daily for 1 week. Percentage of total alive $CD45^+$ cells is shown for CDPs, cMoPs, MDPs, CLPs, LSKs, and $Ly6C^{hi}$ monocytes.

(B and -C) The cutoff on differentially regulated genes considered for the pathway analysis is $p < 0.05$ and pathways are considered deregulated with $p < 0.05$. Shown are –log(p value).

(D–G) Each dot represents one mouse. Shown is mean ± SD. Significance was calculated using Student's t test, $^*p < 0.05$, $^{**}p < 0.01$, $^{***}p < 0.001$. Pool of five experiments (D), two experiments (E), one representative experiment of three out of five that were similar (F), and one representative of two (G) are shown.

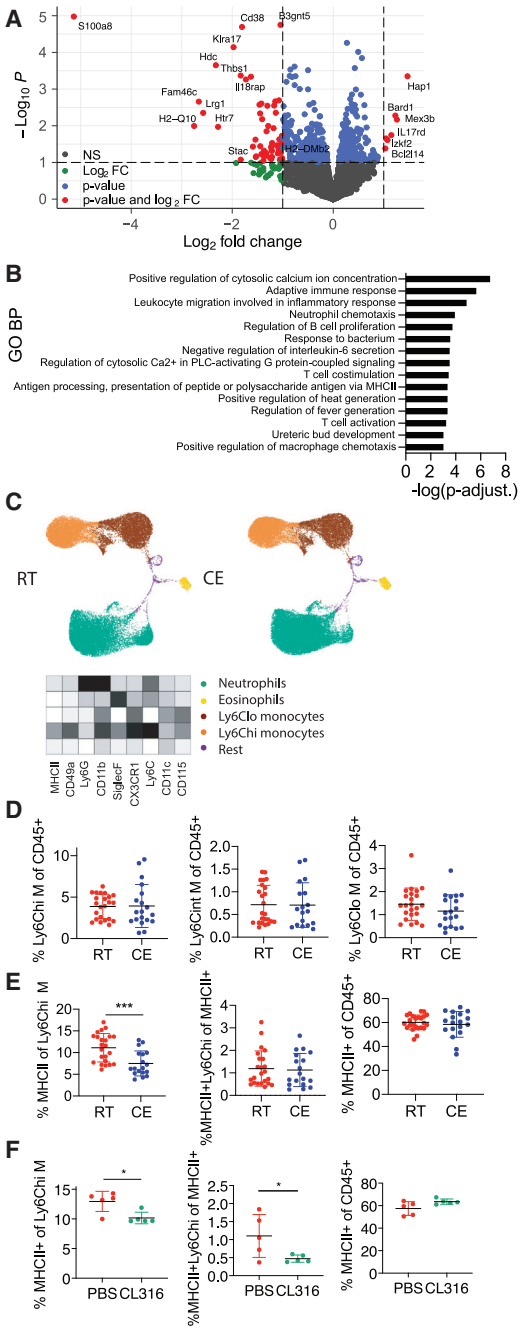


**Figure 2. Cold exposure modulates monocytes in the circulation**

(A) Volcano plot showing the up- and downregulated transcripts by RNA sequencing of monocytes that were MACS (anti-PE) and FACS (CD115-PE+) sorted from blood of 2-week cold-exposed (10°C) mice compared to room-temperature mice.

(B) 15 most enriched Gene Ontology biological processes of monocytes as in (A). Genes were considered differentially regulated with $p < 0.05$. Shown are –log(p value).

(C) Blood immune cells of mice as in (A) visualized using UMAP and clustered using FlowSOM algorithm in R. Ly6C$^{hi}$ monocytes (green), Ly6C$^{lo}$ monocytes (yellow), neutrophils (brown), eosinophils (orange), and others. Heatmap shows median relative expression of all panel markers.

(D) Flow cytometry analysis of blood cells from mice as in (A). Percentage of Ly6C high (hi), intermediate (int), and low (lo) monocytes of total, single CD45$^+$ cells.

(E) Percentage of blood MHCII$^+$ cells of Ly6C$^{hi}$ monocytes (left), MHCII$^+$ Ly6C$^{hi}$ monocytes of total MHCII$^+$ cells (middle), and total MHCII$^+$ cells of total, single CD45$^+$ cells (right) of mice as in (A).

(F) Blood cell analysis after 1 week of daily i.p. injected beta 3 adrenoreceptor agonist CL316,243 or vector (PBS). Percentage of MHCII$^+$ cells of Ly6C$^{hi}$ monocytes (left), MHCII$^+$ Ly6C$^{hi}$ monocytes of total MHCII$^+$ cells (middle), and total MHCII$^+$ cells of CD45$^+$ cells (right).

(D–F) Each dot represents one animal. Shown is mean ± SD. Significance was calculated using Student's t test, *$p < 0.05$, **$p < 0.01$, ***$p < 0.001$. Pool of three experiments (D and E).

out of five experiments, cold exposure decreased the absolute cell numbers (data not shown) and the percentage of monocyte-dendritic cell progenitors (MDPs), common dendritic cell progenitors (CDPs), and tendentially common monocyte progenitors (cMoPs), while the common lymphoid progenitors (CLPs) and most hematopoietic cells (Lin$^-$Sca1$^+$ c-KIT$^+$, also known as LSKs) remained unchanged (Figures 1F and S1E; gating strategy, Figure S1F).

Beta 3-adrenergic receptor signaling is one of the main pathways activated by cold exposure (Cannon and Nedergaard, 2004; Stojanović et al., 2018). The beta 3 adrenoreceptor agonist CL316,243 (CL316) decreased Ly6C$^{hi}$ monocytes, CDPs, and cMoPs (Figure 1G), suggesting that beta 3 adrenoreceptor stimulation is sufficient to partly mimic the effects of cold on the myeloid bone marrow cells and their progenitors. Together, these results suggest that cold exposure decreases myeloid cell progenitors and monocytes in the bone marrow and downregulates monocyte MHCII expression.

## Cold exposure impacts monocytes in blood at steady state

We next examined the systemic relevance of the cold-exposure-mediated changes observed in the bone marrow by fluorescence-activated cell sorting (FACS) of CD115$^+$ blood monocytes (Figure S2A) and subsequently profiling them via RNA sequencing (Figures 2A and S2B). Among the 58 Gene Ontology (GO) biological processes that were enriched, the top 15 terms included leukocyte migration, T cell co-stimulation, and antigen presentation via MHCII (Figure 2B), all processes that are important for the immune system in health and disease. Such pathways were similarly found within the top 15 of 653 total MetaCore Pathway Maps (no p value cutoff) (Figure S2C). MetaCore Metabolic Networks analysis revealed that 13 metabolic terms were enriched (Figure S2D). Among the variety of general cell membrane restructuring elements ($p < 0.05$, total 12), "MHC class II protein complex" was among the most enriched Cellular Components in GO analysis (Figure S2E). To further profile the effect of cold exposure on circulatory immune cells and, in particular, myeloid cells, we performed high parameter flow cytometry (BD FACSymphony), followed by an unbiased analysis using a FlowSOM algorithm (Van Gassen et al., 2015) and visualization via UMAP plots. Overall, we neither observed any major shifts in myeloid cells (Figure 2C) nor in T cell populations (data not shown) or numbers, suggesting that cold exposure induces several gene expression changes on the monocytes without significantly altering the overall immune cell composition. These observations were further supported by flow cytometry, which revealed that cold exposure consistently decreased MHCII

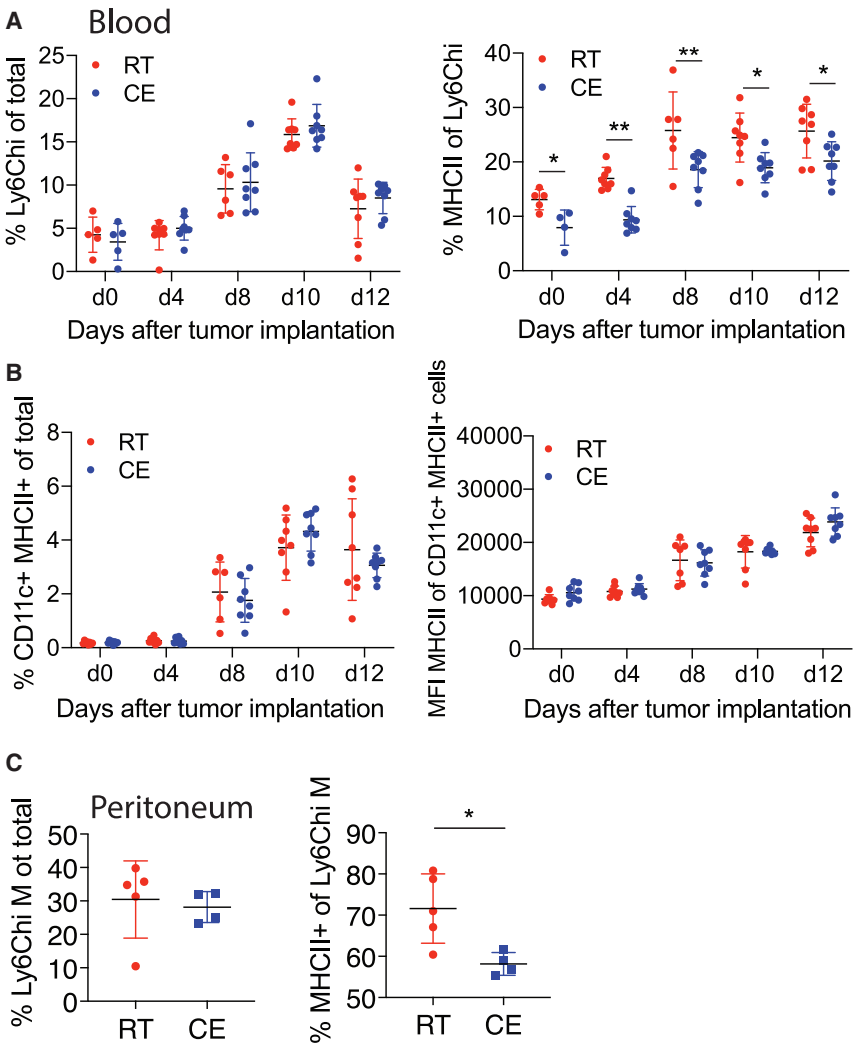


**Figure 3. Cold exposure decreases monocyte MHCII in inflammatory mouse models**

(A) Blood Ly6C$^{hi}$ monocytes and their MHCII expression were analyzed by flow cytometry on different days after B16-GMCSF subcutaneous (s.c). tumor implantation in mice that were cold- (10°C) or room-temperature-exposed for 2 weeks before and during tumor growth.

(B) Blood CD11c$^{+}$MHCII$^{+}$ cells and MHCII mean fluorescence intensity (MFI) of MHCII+CD11c$^{+}$ cells were determined by flow cytometry from mice as in (A).

(C) Flow cytometry analysis of peritoneal fluid cells 24 h after i.p. injection with thioglycollate into 2-week cold-exposed (10°C) or room-temperature mice.

Each dot represents one animal. Shown is mean ± SD. Significance was calculated using multiple t test with Holm-Sidak correction (A and B) or Student's t test (C), *p < 0.05, **p < 0.01.

expression of Ly6C$^{hi}$ monocytes without altering their overall number (Figures 2D, 2E, and S2G; gating strategy, Figure S2F). Similarly, as in the bone marrow, beta 3 adrenoreceptor stimulation mimicked the effects of cold exposure in blood and reduced the MHCII expression of Ly6C$^{hi}$ monocytes (Figure 2F). These data indicate that cold exposure induces functional changes on the monocytes in the blood by reducing their MHCII expression without provoking major changes in the main immune cell populations.

## Cold decreases monocyte MHCII expression in inflammatory mouse models

To study the functional relevance of the observed cold-induced monocyte modulations, we employed various immunologic models. First, we amplified circulating monocytes and their MHCII expression using B16-GM-CSF tumor cells (Dranoff et al., 1993; Menezes et al., 2016) that were subcutaneously injected into cold-exposed or room-temperature-kept mice. GM-CSF initiates an inflammatory phenotype in monocytes, and depletion of monocyte GM-CSF signaling renders mice resistant to EAE (Croxford et al., 2015). Cold exposure decreased MHCII expression of monocytes without changing the monocyte percentage after implantation of the tumor cells (Figure 3A). To confirm that this effect is monocyte specific we also analyzed total CD11c$^{+}$ cells, the majority of which were DCs, and found that they remained unchanged (Figure 3B). Thus, cold exposure decreased MHCII expression on Ly6C$^{hi}$ monocytes in the B16-GM-CSF tumor model.

Next, we triggered a thioglycolate-elicited peritoneal inflammation, in which monocytes were highly attracted into the peritoneum. Cold exposure decreased MHCII expression of recruited Ly6C$^{hi}$ monocytes/monocyte-derived cells within the peritoneum (Figure 3C) without affecting the proportion of several other immune cell populations (Figure S3A). These data show that cold exposure leads to a preferential decrease in the monocyte MHCII expression in various mouse models irrespective of the inflammatory trigger.

Monocytes can acquire antigen-presenting functions, including antigen uptake and migration to the lymph nodes (Guilliams et al., 2018; Jakubzick et al., 2017). We therefore investigated if antigen-presenting functions of monocytes, as well as dendritic cells (Ganguly et al., 2013), might be changed upon cold exposure. For this purpose, we performed an FITC painting assay, in which FITC is applied epicutaneously of one flank of the mouse and allows measuring migratory immune cell properties into the draining lymph node (dLN) (Allan et al., 2006). We monitored the FITC uptake in the ipsi- and contralateral LN at two different time points; 12 h indicates possible initial differences in lymphatic draining, while 18 h is the peak and allows an estimate of the overall changes (Platt et al., 2013). At none of the monitored time points have we observed changes in cell count, FITC uptake, or MHCII expression on dendritic cells, monocytes, and various dendritic cell subsets (Figure S3B; data not shown), thus excluding that cold

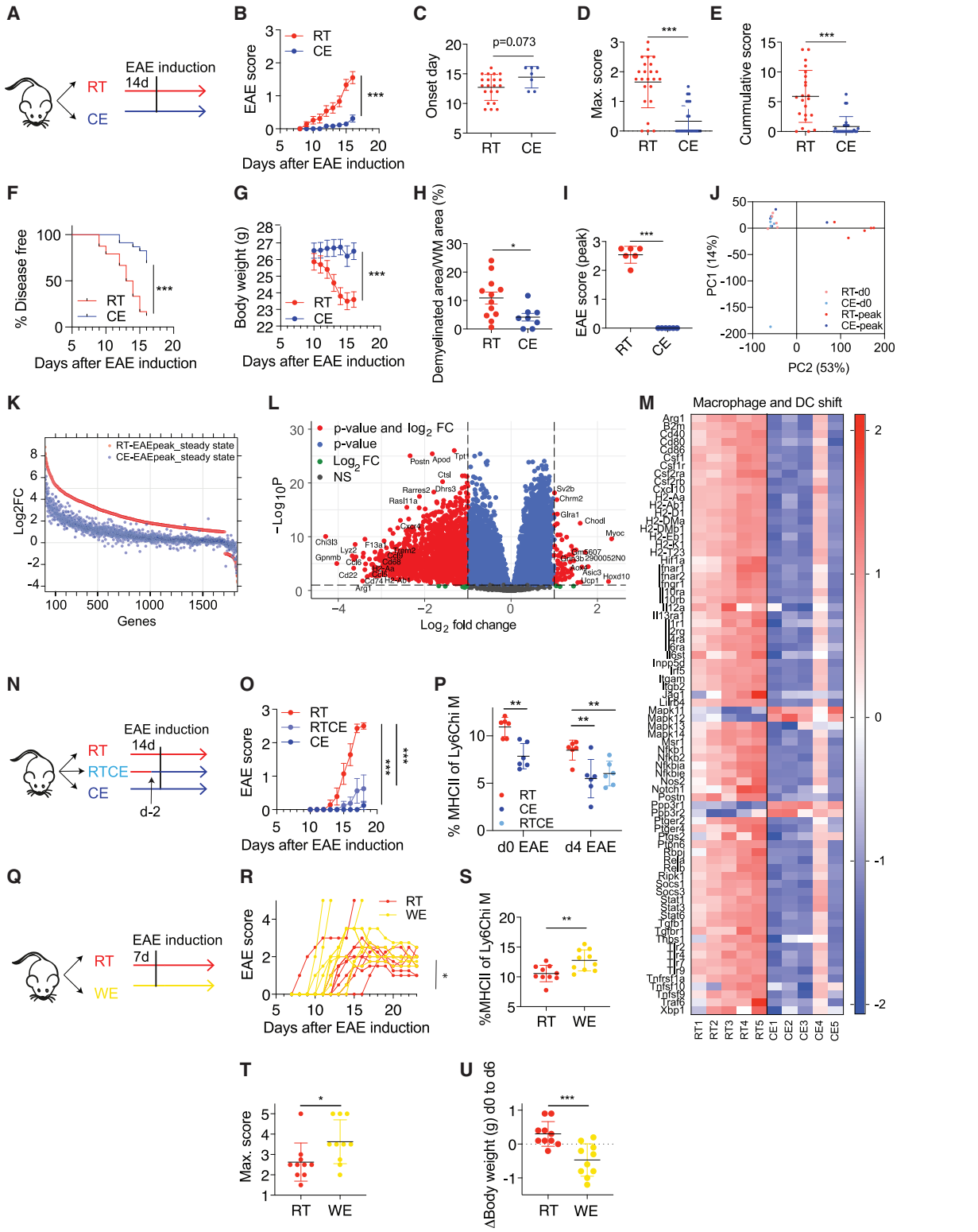


**Figure 4. Cold exposure attenuates neuroinflammation**

(A and B) Scheme showing the experimental setup for EAE and cold exposure (A). EAE was induced by s.c. immunization with MOG35-55 peptide in complete Freund's adjuvant (day 0) and pertussis toxin i.p. (day 0 and 2). Mice were exposed to cold or room temperature (10°C) for 2 weeks before and during EAE. Clinical symptoms of EAE were monitored according to a standardized scoring system (B).

*(legend continued on next page)*

exposure affects antigen drainage to the LN. Altogether, these data show that exposure to lower environmental temperature leads to a decrease in the monocyte MHCII expression in various inflammatory mouse models without affecting the lymphatic drainage.

### Cold exposure attenuates EAE

Monocytes and monocyte-derived cells are important pathogenic players in chronic inflammatory diseases, such as MS. Similarly, monocyte trafficking to the CNS is critical for EAE progression (Ajami et al., 2011; King et al., 2009), and *Ccr2*-deficient mice, which lack monocytes outside the bone marrow (Serbina and Pamer, 2006), show mild (Mildner et al., 2009) or no EAE (Fife et al., 2000; Izikson et al., 2000). We therefore explored whether cold exposure could affect the EAE disease outcome. For this purpose, we exposed mice to 10°C for 2 weeks with an additional initial acclimatization period of 5 days at 18°C and 5 days at 14°C before immunization and kept them at 10°C during the whole EAE (Figure 4A). Strikingly, exposing animals to cold led to a pronounced attenuation of the EAE disease severity compared to room-temperature-kept controls (Figures 4B, S4A, and S4H). The cold-exposed mice also showed delayed onset of the disease, together with a lower maximum and cumulative EAE score, disease incidence, and body weight loss (Figures 4C–4G) compared to the room temperature-kept control mice. Histologic evaluation revealed a reduced area of demyelination (Figure 4H) and a lower number of lesions (Figure S4B) in spinal cords from cold-exposed mice at the peak of EAE. Densities of $Mac3^+$ and $CD3^+$ infiltrates in spinal cords, as well as $APP^+$ axonal spheroides within white matter lesions identified by luxol fast blue/periodic acid shift (LFB/PAS) staining, showed a tendential decrease (Figures S4C–S4G) without reaching statistical significance. As the extent of EAE amelioration slightly differed between experiments, a pool is shown (Figures 4B–4G) of 3 experiments (n = 6–10) performed under the same conditions except the housing room, which had no consistent impact.

To gain insights into the degree of protection by cold exposure on the EAE-induced gene expression changes in the spinal cord, we performed RNA sequencing on mice kept at room or cold temperature both at steady state and at EAE peak. Principle component and multidimensional scaling analysis revealed that when the room-temperature-kept animals reached peak of the disease after EAE induction (Figure 4I), the immunized cold-exposed mice clustered together with the healthy, steady-state animals (Figures 4J and S4I). Interestingly, all genes that were increased in the room-temperature mice with EAE compared to healthy controls were left unchanged or deregulated to a lower extent in the cold-exposed mice under EAE (Figure 4K). These data show that the EAE-provoked spinal cord gene expression alterations are either reduced or prevented by cold exposure. Gene expression comparison between spinal cords from cold-exposed mice versus room-temperature controls during EAE revealed 61 up- and 1,579 downregulated genes of 15,467 total genes ($p < 0.05$; logFC > 1) (Figure 4L). Among the top 984 regulated pathways identified by the MetaCcore Pathway Maps, "Macrophage and Dendritic cell phenotype shift" was the most significantly changed one. This pathway includes MHCII genes and other activation markers (Figures 4M and S4J), further indicating that the myeloid cell and antigen presentation are the most prominent changes induced by cold also during EAE. The pathway analysis further revealed downregulation of CXCL10, a recently identified marker of a pathogenic monocyte subset (Giladi et al., 2020), which we found similarly decreased in the bone marrow (Figure 1C).

To investigate whether the length of the cold exposure before the EAE induction is important for the EAE onset and disease progression, we pre-exposed mice to cold 2 days before immunization and compared them to the animals that were kept 2 weeks at 10°C as in the standard protocol. Two days of cold pre-exposure was sufficient to attenuate EAE, although to a slightly lower extent than 2 weeks of pre-exposure (Figures 4N and 4O), and to reduce monocyte MHCII (Figure 4P), suggesting that the length of the cold pre-treatment plays a modest role in the disease outcome.

To address whether warm exposure has an opposing effect on EAE, we exposed mice to 34°C for 7 days before immunization and kept them warm during EAE (Figure 4Q). Warm exposure led to decreased food intake and body weight (Figures 4O, 4U, S4M, and S4N). Although more mice died under warm exposure, the survival rate was not significantly different, and neither was the day of onset (Figures S4O and S4P). However, in contrast to the effects seen during cold, the MHCII expression of $Ly6C^{hi}$

(C–G) Day of EAE onset, i.e., when first symptoms occur (C); maximum disease score, i.e., the highest score an individual mouse reached during the experiment (D); cumulative disease score, i.e., the sum of all scores each individual mouse reached during the experiment (E); and the percentage of disease-free mice (F) and body weight (G) of mice as in (A).

(H) Quantification of demyelinated area expressed as percentage of white matter (WM) detected by Luxol Fast Blue and periodic acid-Schiff (LFB-PAS) of spinal cords from mice as in (A).

(I–M) Spinal cords of healthy and peak EAE mice that were kept at room temperature or cold exposed for 2 weeks were used for RNA sequencing. Scores of the respective mice at sacrifice (I), principal component analysis (J), relativeness analysis of logFC of room temperature healthy versus EAE spinal cords (red) and cold exposure healthy versus EAE spinal cords (blue) with $p < 0.05$ and FC > 2 (K), volcano plot (gene *Gpx3* was excluded for better visualization) (L), and genes of top1 deregulated pathway "Macrophage and DC phenotype shift in cancer" from MetaCore Pathway Maps with $p < 0.05$ (M).

(N and O) Scheme showing the experimental setup. Mice were exposed to cold temperature for either 2 weeks or 2 days before and continued during EAE and compared to room temperature controls (N). EAE was induced as in (A) and EAE scores are shown (O).

(P) Percentage of MHCII expression on $Ly6C^{hi}$ blood monocytes was determined using flow cytometry on day 0 and day 4 after EAE induction.

(Q and R) Scheme showing the experimental setup (Q). Mice were exposed to warm temperature of 34°C for 1 week before and during EAE (as in A) and compared to room temperature controls. Each curve represents one individual mouse (R).

(S) Percentage of MHCII expression of $Ly6C^{hi}$ blood monocytes from mice as in (Q) was determined using flow cytometry on day 0 of EAE.

(T and U) Maximum disease score (T) or delta of body weight gain from day 0 to day 6 of warm exposure (U).

(B–S) Data (B–G) represent pool of 3 experiments (n = 6–10 mice per group per experiment). Shown is mean ± SEM, two-way ANOVA (B, G, O, and R), Student's t test (C–E, I, and S–U), Mantel-Cox (F), multiple t test with Holm-Sidak correction (P), *$p < 0.05$, **$p < 0.01$, ***$p < 0.001$.

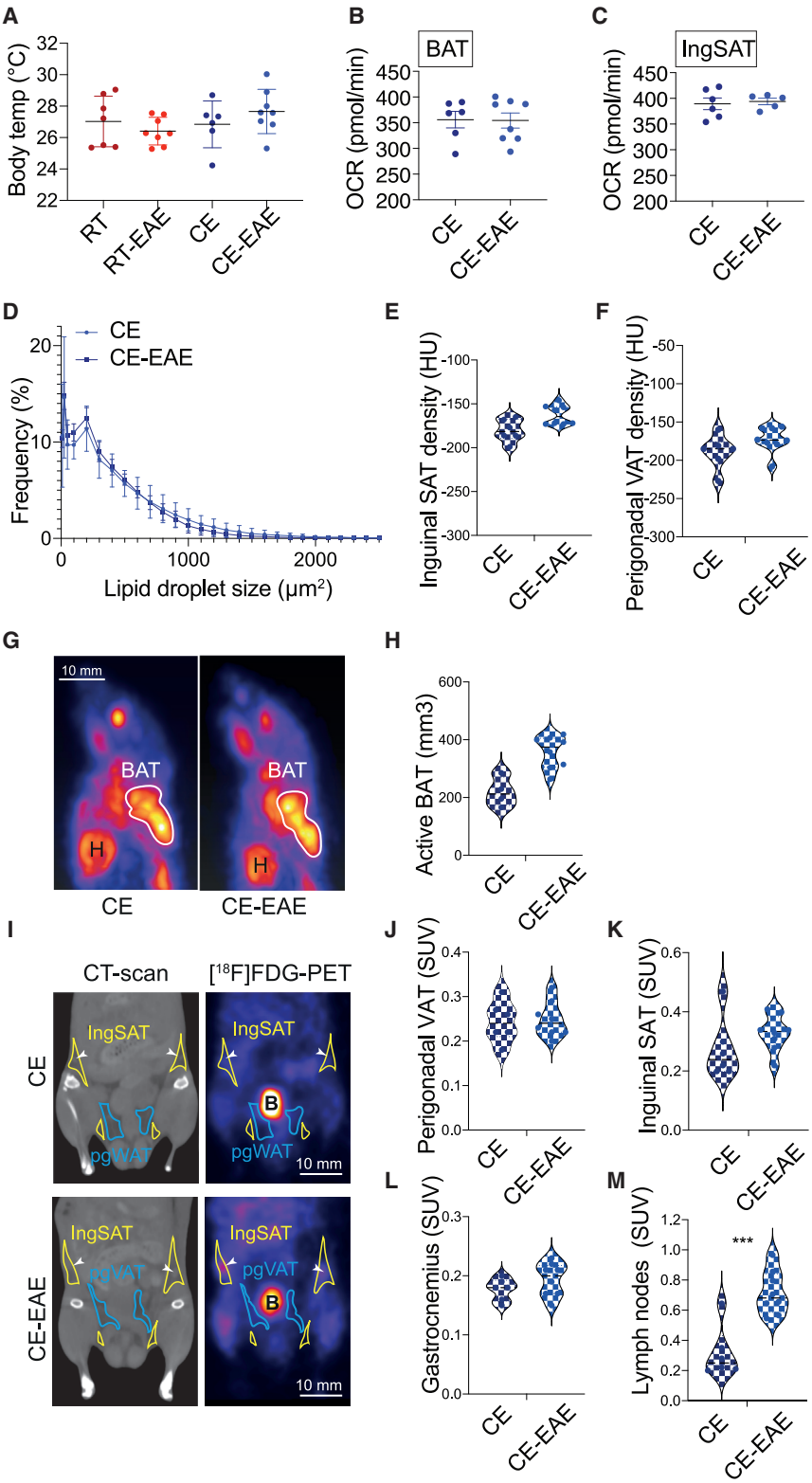


**Figure 5. The thermogenic response and resource allocation are not reduced by EAE**

(A) Body temperature shown as the mean temperature of the two eyes as determined via infrared images of mice on day 7 of EAE. Mice were cold exposed for 2 weeks before and during EAE or steady state. Control mice were at room temperature for the same duration.

(B and C) Oxygen consumption rate of interscapular brown (BAT; B) and inguinal subcutaneous adipose tissue (ingSAT; C) on day 8 of EAE or in steady state after 3 weeks of cold exposure (CE) and 3 h of fasting.

(D) Quantification of lipid droplet size distribution in inguinal SAT. Slides were analyzed in technical duplicates from different layers of the tissue and averaged.

(E and F) Density of the inguinal SAT (E) and perigonadal VAT (F) shown in Hounsfield units from mice as in (A).

(G and H) Maximum intensity projection of [$^{18}$F]FDG-PET scans of one representative mouse per group (G) and active BAT volume (mm$^3$) (H) of mice as in (A)

(I–M) Coronal views and [$^{18}$F]FDG-PET scans of one representative mouse per group (I) and standardized uptake values (SUVs) of radiolabeled tracer 2-deoxy-2-[$^{18}$F]fluoro-D-glucose ([$^{18}$F]FDG) in perigonadal VAT (J), inguinal SAT (K), gastrocnemius muscle (L), or inguinal lymph nodes (M) of mice as in (A).

Multiple t test with Holm-Sidak correction (A) or Student's t test (B–F, H, and J–M). Data are shown as mean ± SD; each round dot represents one animal (n = 6–8 mice per group). *p < 0.05, **p < 0.01, ***p < 0.001. B, bladder; H, heart. White arrows point to the inguinal lymph nodes.

monocytes was increased in the warm-exposed mice, coupled with deteriorated EAE, enhanced body weight loss, and increased maximum disease score (Figures 4R–4T, S4K, and S4L). Together, these results suggest that the temperature is a critical determinant for EAE severity and that cold exposure is a potent stimulus that attenuates neuroinflammation.

Long-term cold exposure increases energy expenditure by enhancing the thermogenesis in the brown and beige fat, enabling homeothermy (Chevalier et al., 2015). However, when additional biologic maintenance programs are active, as in inflammation, we hypothesized that these responses (maintenance of homeothermy and autoimmunity) may be in competition for energy. We therefore analyzed a variety of parameters involved in thermogenesis in the cold-exposed groups of mice. There was no difference in the body temperature between the room-temperature-kept or cold-exposed healthy versus EAE mice (Figure 5A). While kept under room temperature conditions, EAE reduced the blood glucose levels; 3 h fasting glycemia during cold was unchanged between EAE and healthy mice (Figure S5A). To further address the functional properties of the BAT and SAT during cold, we studied the oxygen consumption rates, which were

CellPress
OPEN ACCESS

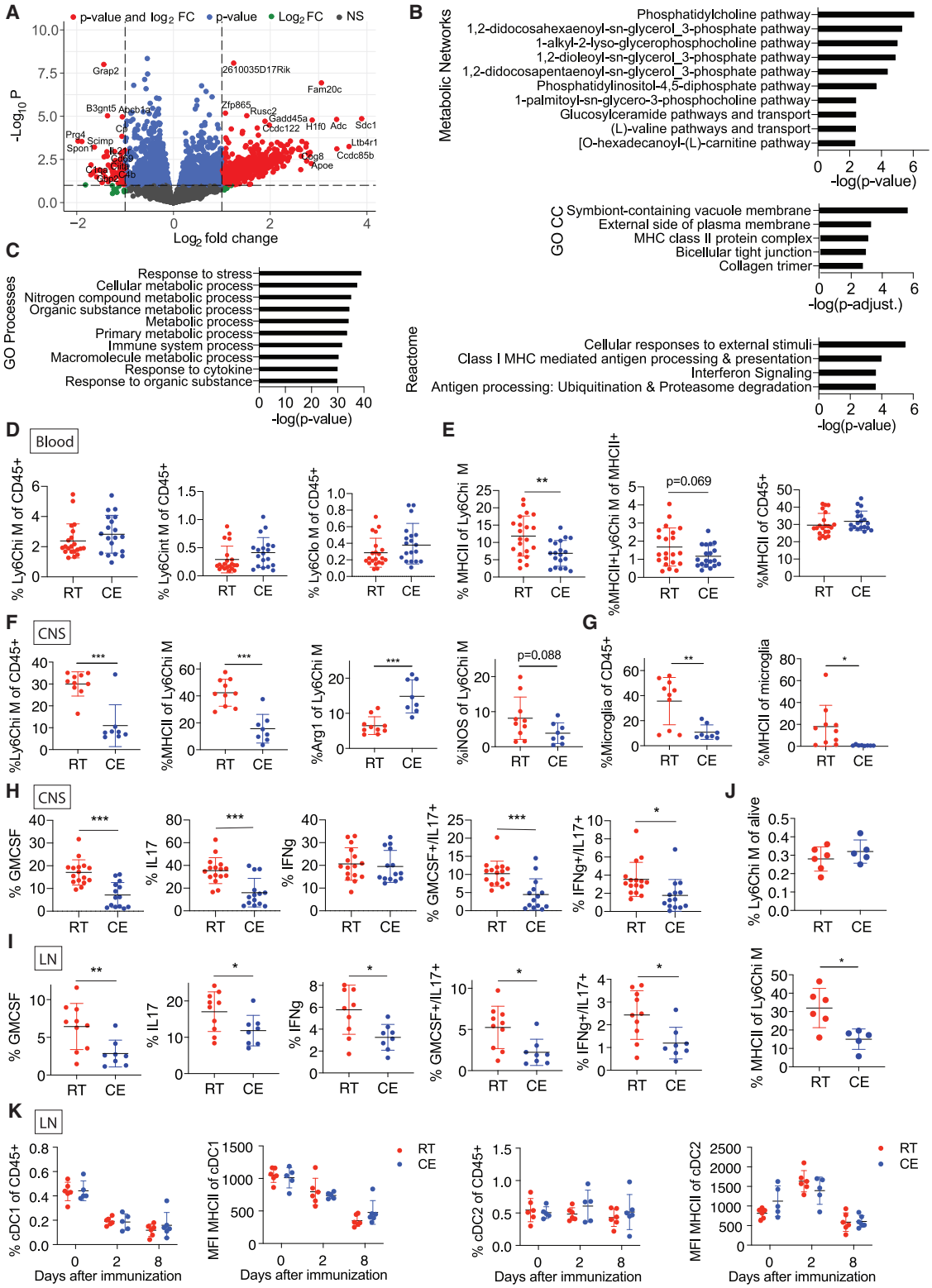


**Figure 6. Cold exposure reduces monocyte and T cell pathogenicity during EAE**

(A) Volcano plot identifying the up- and downregulated transcripts after RNA sequencing of monocytes that were MACS (anti-PE) and FACS (CD115-PE$^+$) sorted from blood of mice at onset of EAE (as in Figure 4A) and exposed to cold (10°C) or room temperature for 2 weeks before and continued during EAE.

(B and C) Top deregulated and enriched MetaCore Metabolic Networks (B, top), GO Cellular Components (B, middle), Reactome pathways (B, bottom), and GO processes (C). Genes were considered when $p < 0.05$ and for Reactome pathways when $p < 0.05$ and FC > 2. Data of sequencing as in (A).

*(legend continued on next page)*

similar between the cold-exposed EAE and healthy mice in both inguinal SAT and BAT (Figures 5B and 5C). Consistent with the lack of functional differences, the weights of the BAT and inguinal SAT depots of the EAE mice compared to the healthy cold-exposed controls were unchanged (Figures S5B–S5D). While the expression of *Cidea* and *Pparg* in the BAT was reduced in the cold-exposed EAE mice, the rest of the brown fat markers were unaltered, and there was no difference in expression in any of the browning markers in the inguinal SAT (Figures S5E and S5F). Moreover, we detected no changes in the lipid droplet size distribution between cold-exposed healthy or EAE mice (Figure 5D), together suggesting no detectable EAE-induced limitation of the BAT and SAT thermogenic response during cold. However, the slightly milder BAT marker activity under EAE, but without overall reduction in the thermogenesis and oxygen consumption rates, may suggest competition for energetic resources between of the two energy-costly programs. This lack of functional limitations in the thermogenic response, coupled with the decreased neuroinflammation during cold, indicate prioritization of the homeothermic over autoimmune response, resulting in ameliorated EAE. To further compare the possible energetic allocation from the metabolic tissues in response to EAE during cold, we used positron emission tomography-computer tomography (PET-CT) in two groups of cold-exposed mice—with or without EAE induction—allowing us to monitor if introducing the autoimmune trigger would shift resources away from the thermogenic tissues before the disease onset. In line with the lipid droplet size distribution data, we found no differences in the densities of both inguinal and perigonadal adipose tissues between cold and cold-EAE mice (Figures 5E and 5F). The [$^{18}$F]fluorodeoxyglucose ([$^{18}$F]FDG) uptake in BAT during cold was even slightly elevated rather than being reduced by EAE, suggesting that the resource allocation to the thermogenic tissues is not suppressed by the autoimmune activation. Similarly, we neither observed changes in the [$^{18}$F]FDG uptake in gastrocnemius nor found a decrease in the perigonadal VAT and inguinal SAT glucose uptake (Figures 5G–5L). In contrast, the cold-exposed EAE group showed profound increase in the glucose uptake in the lymph nodes compared to the cold-kept controls (Figure 5M). Together, these data demonstrate that the resource allocation to the thermogenic tissues, as well as their thermogenic responses, are ensured despite the EAE.

Cold exposure activates BAT thermogenesis primarily through UCP1, which uncouples the mitochondrial respiratory chain from the ATP biosynthesis. However, during prolonged acclimatization to cold, the *Ucp1*-knockout (KO) mice are able to compensate for the lack of UCP1 through additional UCP1-independent thermogenic mechanisms that can satisfy the thermogenic needs, but at a very high energetic cost (Ikeda et al., 2017). Surprisingly, *Ucp1* deletion rendered mice even more protected from EAE compared to their wild-type (WT) littermates (Figure S5G), associated with increased body weight of the *Ucp1*-KO compared to their WT littermates during cold and EAE, consistent with the overall improved health status. These data demonstrate that the UCP1-dependent BAT activity is dispensable for these effects. They also show that cold exposure ameliorates EAE but without a cost to the overall homeothermic response.

## Cold exposure decreases monocyte and T cell pathogenicity during EAE

Monocytes play an essential role in EAE development, progression, and remission (Ajami et al., 2011; Fife et al., 2000; Izikson et al., 2000; King et al., 2009; Mildner et al., 2009; Serbina and Pamer, 2006), and they reach the CNS in inflammatory conditions through the blood stream. To examine whether cold exposure affects monocytes in the circulation during EAE, we performed RNA sequencing on blood monocytes after FACS sorting (Figures S6A and S6B) at the EAE onset. Fold change analysis ($p < 0.05$, logFC > 1) revealed 660 up- and 86 downregulated genes of 10,794 total genes (Figure 5A) in cold-exposed compared to room-temperature mice. MetaCore Metabolic Network analysis ($p < 0.05$) showed 23 enriched networks (Figure 6B). Among the 3,366 enriched terms identified using MetaCore GO, the top 10 terms were mainly metabolic changes (Figure 6C). Interestingly, Gene Ontology Cellular Components identified "MHC class II protein complex" among the top 5 of 10 total enriched terms (Figure 6B, middle). Within the Reactome pathway analysis, pathways important for antigen presentation were within the 4 identified hits (Figure 6B, bottom).

The changes in MHCII antigen presentation machinery in blood monocytes at EAE onset between the cold-exposed and the room-temperature mice were confirmed by flow cytometry (Figure S6C). While the percentage and number of Ly6C$^{hi/int/lo}$ monocytes remained the same (Figures 6D and S6D), cold exposure led to decreased MHCII of Ly6C$^{hi}$ monocytes, coupled to a partial lowering ($p = 0.069$) in the percentage of MHCII$^{+}$Ly6C$^{hi}$ M within the total MHCII$^{+}$ cells but no change in the percentage of total MHCII expression of CD45$^{+}$ cells (Figure 6E). Blood and lymph node immune cells at different days of EAE were further investigated using high dimensional flow cytometry and unbiased computed analysis, and we detected no alterations, thus excluding changes in the myeloid cell populations (Figures S6E and S6F). These analyses demonstrate that cold exposure

(D and E) Flow cytometry analysis of blood cells of mice as in (A) at EAE onset. Percentage of Ly6C high (left), intermediate (middle), and low (right) monocytes of total, single CD45$^{+}$ alive cells (D). Percentage of MHCII$^{+}$ cells of Ly6C$^{hi}$ monocytes (left), MHCII$^{+}$ Ly6C$^{+}$ monocytes of total MHCII$^{+}$ cells (middle), and total MHCII$^{+}$ cells of CD45$^{+}$ cells (E). Pool of 3 experiments.

(F–H) Flow cytometry analysis of CNS cells from mice as in (A) at EAE onset. Percentage of Ly6C$^{hi}$ monocytes/monocyte-derived cells of total, single CD45$^{+}$ alive cells (F, left). Percentage of MHCII, arginase 1 (Arg1), and iNOS expression of Ly6C$^{hi}$ monocytes/monocyte-derived cells (F, right). Percentage of microglia of total, single CD45$^{+}$ alive cells and percentage of MHCII of microglia (G). Percentage of corresponding cytokine expression as indicated in CD4$^{+}$ T cells (H).

(I) Flow cytometry analysis of dLN cells from mice as in (A) at EAE onset. Percentage of cytokine expression in CD4$^{+}$ T cells. Observed in 2 out of 3 experiments.

(J) Flow cytometry analysis of dLN cells from mice as in (A) on day 2 after EAE induction. Percentage of Ly6C$^{hi}$ monocytes of total, single CD45$^{+}$ alive cells (upper panel). Percentage of MHCII on Ly6C$^{hi}$ monocytes (lower panel).

(K) Flow cytometry analysis of lymph node (LN) dendritic cells (DCs) and their MFI of MHCII on different days after immunization.

(D–K) Shown is mean ± SD; significance was calculated using Student's t test, *$p < 0.05$, **$p < 0.01$, ***$p < 0.001$. Shown is 1 representative example of 3 (F), a pool of 2 experiments (H), or one representative experiment of two out of three that were similar (I).

reduced MHCII expression of circulating Ly6C$^{hi}$ monocytes at EAE onset without shifting myeloid cell populations.

Circulating Ly6C$^{hi}$ monocytes contribute to EAE pathology by migration to the inflamed CNS (Ajami et al., 2011; Fife et al., 2000; Izikson et al., 2000; King et al., 2009; Mildner et al., 2009; Serbina and Pamer, 2006). We therefore investigated if the changes detected in the circulating monocytes may be seen within the inflamed CNS at EAE onset. Cold exposure decreased the percentage of Ly6C$^{hi}$ monocytes/monocyte-derived cells and their MHCII expression within the CNS (Figure 6F). Furthermore, their Arg1 expression was increased, indicating a predominant anti-inflammatory M2-like phenotype (Figure 6F). Percentage and MHCII expression of microglia were similarly decreased (Figures 6G and S6G), together suggesting that they are activated to a lower extent at EAE onset under cold exposure.

Apart from monocytes and monocyte-derived cells, T cells are the main drivers of EAE pathogenicity. Cold exposure led to a decrease of pathogenic T cell cytokine signature and a reduction of GM-CSF/IL-17 and IFNg/IL-17 double producers in the CNS (Figure 6H). We detected similar changes in the dLN (Figure 6I), whereas in the mesenteric lymph nodes, only GM-CSF was decreased (Figure S6H, upper), and no changes were seen in the spleen (Figure S6H, bottom). Further, no changes were detected for regulatory T cells (Figure S6I). In the dLN, MHCII expression of Ly6C$^{hi}$ monocytes was lower on day two (Figure 6J), but not at onset of EAE or at steady state (data not shown). There were no consistent differences in dendritic cell populations or their activation status in the dLN at any time (Figure 6K). Collectively, these data show that cold exposure attenuates Ly6C$^{hi}$ monocyte and T cell pathogenicity during active EAE.

### T cell priming by monocytes is critical for the cold-induced attenuation of EAE

The described changes in two of the main pathogenic cell types mediating EAE provide mechanistic support for the observed amelioration of EAE by cold exposure. We therefore investigated what the connection is between monocytes and T cells during cold and EAE. Since cold exposure reduced T cell cytokine expression early during EAE and the monocyte changes were already detected under steady-state conditions, we raised the questions of whether cold exposure affects the priming of T cells and what the role of monocytes is at regulating this stage. To investigate this, we used an adoptive transfer model for passive EAE induction, in which *in vitro* Th1-polarized, transgenic, MOG-specific 2D2 T cells were injected into room-temperature or cold-exposed mice (Figure 7A). Similar to the active EAE, cold exposure reduced MHCII expression of Ly6C$^{hi}$ blood monocytes during the passive EAE onset after transfer of differentiated 2D2 cells, while monocyte percentages remained unchanged (Figures 7B–7E). Priming T cells *in vitro* completely abolished the cold-exposure-induced amelioration of EAE (Figures 6F–6K, upper). Similar results were obtained after adoptive transfer of Th17 differentiated cells (Figures 7F–7K, bottom). These data suggest that the effects of cold exposure during the T cell priming phase are critical for the attenuation of EAE and that cold-exposure-mediated MHCII downregulation may be responsible for these effects. These conclusions were supported with data from cold-exposed mice that were shifted to room temperature on the day of immunization. Transferring cold-exposed mice to room temperature prior to the T cell priming stage (Figure S7A) abolished the cold-induced effects on the active EAE disease (Figure S7B) and MHC expression on monocytes (Figure S7C). This is in agreement with the observation that the MHCII downregulation in monocytes under cold exposure was not sufficient to ameliorate EAE following adoptive transfer of pre-activated encephalitogenic T cells, thus making it unlikely that the observed monocyte changes are downstream mediators of effector T cells.

To directly test whether monocytes may influence T cells during their priming phase in cold, we used two complementary approaches to deplete peripheral monocytes: anti-CCR2 (MC-21) antibody and *Ccr2*-KO mice, both of which restrict monocytes to the bone marrow (Serbina and Pamer, 2006). While anti-CCR2 completely abolished peripheral blood monocytes 2 days before EAE onset, *Ccr2*-KO mice showed significant but incomplete loss of monocytes from the blood (Figure 7L), likely because during inflammation, there could be a compensatory, CCR2-independent mechanisms for partial monocyte exit from the bone marrow. While cold exposure decreased pathogenic T cell cytokine expression in the isotype control mice, both monocyte-depletion mouse models did not show any T cell cytokine expression in the dLN (Figure 7M) irrespective of the housing temperature. Together, these data show that monocytes play a critical role in T cell priming with subsequent implications on the T cell encephalitogenic capacities.

## DISCUSSION

Our study has several fundamental implications for understanding the immune system functioning in relation to an energy-demanding metabolic stimulus, such as the change in the environmental temperature. The work provides a systematic overview of the immune cell changes in bone marrow and blood as a consequence of cold exposure during steady state and shows that lower environmental temperature markedly ameliorates neuroinflammation. The cold-induced gene expression alterations were accompanied by phenotypic and functional changes of monocytes. Reduced MHCII expression and related pathways in these cells were accompanied with lowered antigen-presenting capacity following various inflammatory stimuli. This cold-induced monocyte modulation resulted in reduced priming of autoreactive T cells, leading to attenuated autoimmune CNS disease. These data reveal a hitherto underestimated role of monocytes during T cell priming in autoimmunity.

Circulating Ly6C$^{hi}$ monocytes can acquire antigen-presenting functions and can exert pro- and anti-inflammatory tasks (Jakubzick et al., 2017). They therefore play an important role during infections but are also involved in autoimmune pathogenesis. The importance of monocytes and monocyte-derived cells during the effector phase of EAE is well established (Fife et al., 2000; Izikson et al., 2000; King et al., 2009; Serbina and Pamer, 2006), in particular, the relevance of migration of *Ccr2*$^{+}$ monocytes into the CNS (Fife et al., 2000). This is in line with our observation that cold exposure reduces monocyte-derived cells during EAE in the CNS. However, our data also point out that the noted ameliorated EAE disease under cold exposure was

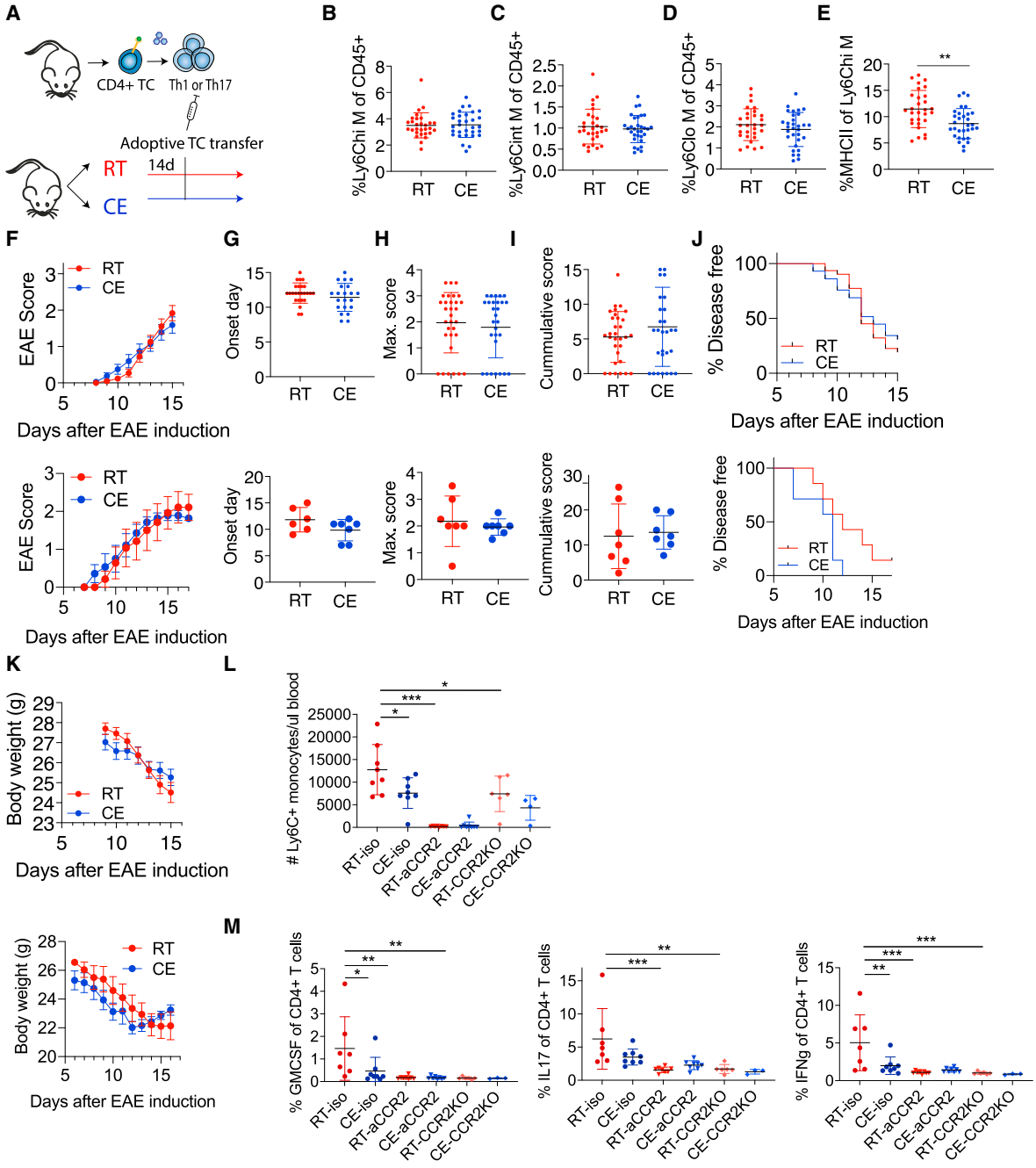


**Figure 7. Monocyte regulation of the T cell priming is critical for cold-induced EAE attenuation**

(A) Scheme showing experimental setup for cold exposure and adoptive transfer EAE. T cells from transgenic 2D2 mice or actively immunized WT donor mice were *in vitro* differentiated toward Th1 or Th17, respectively, and transferred into room-temperature or cold-exposed (2 weeks, 10°C) mice.

(B–E) Flow cytometry analysis of blood cells of mice as in (A) at EAE onset. Percentage of Ly6C$^{hi}$ (B), intermediate (C), and low monocytes of total, single CD45$^{+}$ cells (D). Percentage of MHCII$^{+}$ cells of Ly6C$^{hi}$ monocytes (E).

(F–K) EAE symptoms of mice as in (A) were scored (F). Onset day of EAE disease (G), maximum score (H), cumulative score (I), percentage of disease-free animals (J), and body weight (K). All panels are shown following adoptive transfer of Th1 (upper) and Th17 (lower) cells.

(L and M) Isotype control antibody, CCR2 antibody injected, or *Ccr2*-knockout (KO) mice were housed at room temperature or cold (10°C) for 2 weeks before and during EAE and were s.c. immunized with MOG35-55 peptide in complete Freund's adjuvant. Two days before disease onset, monocyte depletion efficiency was analyzed in the blood (L) and at onset T cell cytokine expression in the draining lymph nodes (M) via flow cytometry. Data represent mean ± SD; significance was calculated using multiple t test with Holm-Sidak correction, *p < 0.05, **p < 0.01, ***p < 0.001.

(B–E, F–K, L, and M) Pool of 3 experiments (B–E and F–K, upper panel). Student's t test with mean ± SD (B–E and G–I), two-way ANOVA with mean ± SEM (F and K), or Mantel-Cox (J). Multiple t tests with Holm-Sidak correction with mean ± SD, *p < 0.05, **p < 0.01, ***p < 0.001 (L and M).

associated with a reduced generation of encephalitogenic T cells, which was most prominent during the early phase of the disease. This suggests a cold-induced effect on the priming of naive autoreactive CD4+ T cells, since adoptive transfer of *in vitro* pre-activated 2D2 T cells abolished the observed protection on EAE. While dendritic cells are supposed to be the primary antigen-presenting cells involved in T cell priming (Ganguly et al., 2013; Steinman and Banchereau, 2007), we did not find indications that cold exposure impacted dendritic cell function per se. Instead, our data rather suggest that altered monocytic function was implied in the reduced priming of autoreactive T cells under cold. Although it is known that monocytes can present antigens to T cells, their role in the context of CNS autoimmunity for T cell priming remains debated (Guilliams et al., 2018; Jakubzick et al., 2017). One previous study (Ko et al., 2014) described decreased, but not abrogated, IL-17 expression in *Ccr2*-DTR mice at EAE onset and did not report differences in IFNg or GM-CSF. However, the *Ccr2*$^{+}$ cell depletion was induced transiently and after immunization and therefore likely did not address the initial priming phase. Another study found a minor decrease in IFNg/GM-CSF double producing CD4$^{+}$ T cells but no abrogation and no effect on IL-17 in *Ccr2*-KO mice before EAE onset (Ronchi et al., 2016). This mild effect on T cell pathogenicity could likely be explained by the experimental conditions or by an incomplete monocyte depletion from the circulation in the *Ccr2*-KO mice under inflammatory conditions. Indeed, the monocyte depletion in our study was milder in the *Ccr2*-KO compared to the anti-CCR2-treated mice. We observed complete abrogation of pathogenic T cell cytokines after acute depletion of monocytes using the antibody-mediated approach—effects also evident in our genetic, *Ccr2*-KO mice.

In addition to the decrease in monocyte-derived cells, cold exposure led to reduction of monocyte MHCII expression in bone marrow, blood, and CNS at steady state or during the early phase of EAE, which provides a mechanistic link to the observed reduction in T cell priming and consequently ameliorated disease course. The fact that MHCII in monocytes remained reduced even after adoptive transfer of pre-activated 2D2 cells that abrogated the protective effect of cold on EAE strengthens the conclusions that the cold-induced monocyte changes interfere upstream of T cell effector cells. We excluded other potential mechanisms by which monocytes could affect T cell priming; neither the uptake and transport of antigen by monocytes in FITC-painted mice nor monocyte cytokine expression on transcriptional level at steady state and EAE onset were modified under cold. Previous studies have suggested a positive feedback loop between T cells and monocytes, where T cells secrete GM-CSF to induce monocyte IL-1b expression (Croxford et al., 2015), which in return amplifies expansion of GM-CSF$^{+}$ Th17 cells (Mufazalov et al., 2017). Our study adds an additional layer to this feedback loop, stressing that as an initial step, monocyte MHCII is critical for T cell priming.

Cold exposure induces beta-adrenergic stimulation of the BAT to activate lipolysis, glucose uptake, and mitochondrial biogenesis and is extensively studied in context of obesity and metabolic disorders (Jastroch, 2017). Cold-induced BAT activation and white fat browning result in a thermogenic response that is energy demanding. As such, this metabolic response may require an energetic trade-off that competes with other energy costly programs, for instance, immune responses (Wang and Medzhitov, 2019). Several studies address the energy trade-off concept in the context of immune defense during infections and found that energy-conserving hypometabolic states may favor the utilization of tissue tolerance as a defense against bacterial pathogens (Ganeshan et al., 2019; Weis et al., 2017). Similar to cold, caloric restriction also induces negative energy balance, reduces and modulates circulating monocytes (Jordan et al., 2019), and lowers CNS monocytes and their pathogenicity (Cignarella et al., 2018; Piccio et al., 2008). In contrast to caloric restriction, which requires an intervention to reduce food intake, cold exposure ameliorates EAE despite the excessive caloric uptake. Certainly, a competition between thermogenesis and a destructive immune response would be favorable with regard to autoimmune diseases, as we see in our study. It was speculated that at low temperatures, defense of remaining thermogenesis over immunity may take place (Wang and Medzhitov, 2019). Our study is in line with this scenario and shows that cold exposure dampens autoimmunity, thus providing evidence and a conceptual advance in our understanding of the energetic trade-off at the cost of autoimmunity. In support of these conclusions, cold exposure ameliorates EAE to a higher extent in absence of UCP1 and following acclimatization and activation of the UCP1-independent thermogenic mechanisms, which function at a very high energetic cost (Ikeda et al., 2017; Reynés et al., 2019; Roesler and Kazak, 2020). The cold-induced immune changes seem to originate already in the bone marrow and can be partially provoked by beta-adrenergic agonism, which may suggest contribution of the nervous system to the energy trade-off. With regard to this concept, it is important to stress that while evidently protective against autoimmunity, cold exposure increases susceptibility to certain viral infections (Foxman et al., 2015; Jaakkola et al., 2014). Thus, our work could be relevant not only for CNS autoimmunity but also other immune-mediated or infectious diseases, which warrants further investigations.

Our study reveals that cold exposure orchestrates immunologic reprogramming that protects from CNS autoimmunity, showing that monocytes and the monocyte MHCII expression are crucially implicated during T cell priming in the course of an autoimmune response. These findings provide critical insights into the pathogenic mechanisms of neuroinflammation and could lead to future preventive and therapeutic approaches for MS and other autoimmune diseases.

## Limitations of study

While we highlight the potential implication of MHCII-expressing monocytes during T cell priming in the course of neuroinflammation, the current work does not investigate the upstream mechanisms by which energetic disbalance induced by cold causes these effects. We observed that beta-adrenergic stimulus decreases the Ly6Chi monocytes; however, it is likely that additional local or systemic upstream signals also contribute to the altered monocyte function and the ameliorated EAE outcome during cold. Moreover, while previous work has shown that cold exposure may have immunomodulatory effects in healthy humans (Kox et al., 2014), the direct human applicability of the findings that energetically costly stimulus ameliorates neuroinflammation remains to be established.

## STAR★METHODS

Detailed methods are provided in the online version of this paper and include the following:

- KEY RESOURCES TABLE
- RESOURCE AVAILABILITY
  - Lead contact
  - Materials Availability
  - Data and Code Availability
- EXPERIMENTAL MODEL AND SUBJECT DETAILS
  - Mice
- METHOD DETAILS
  - EAE induction and scoring
  - B16-GMCSF tumor and thioglycolate elicited peritoneal inflammation
  - FITC migration of DCs using skin painting of the flank
  - Antibody treatment for CCR2$^{+}$ monocyte depletion
  - Positron emission tomography – computer tomography (PET-CT)
  - Histology
  - Immune cell isolation from tissues
  - Flow cytometry
  - Oxygen Consumption Rate (OCR)
  - RNA extraction for RNA sequencing and qPCR
  - Blood monocyte purification for RNA sequencing
  - RNaseq sequencing and analysis
- QUANTIFICATION AND STATISTICAL ANALYSIS

## SUPPLEMENTAL INFORMATION

Supplemental information can be found online at https://doi.org/10.1016/j.cmet.2021.10.002.

## ACKNOWLEDGMENTS

We thank the iGE3 Genomics Platform at the University of Geneva for mRNA sequencing and mapping reads; the Flow Cytometry core facility at the CMU of the University of Geneva for help with flow cytometry; Christelle Veyrat-Duberex, Florian Visentin, Melis Colakoglu, Giovanni di Liberto, Salvatore Fabbiano, Karim Hammad, and Jing Xue for experimental assistance; Sergei Startchik for the help on automatized lipid droplet quantification; Stephanie Hughes and Pierre Guermonprez for organizing and providing B16-GMCSF cells, respectively; Thomas Korn for the Th17 EAE protocol; and Claes Wollheim for discussions. Some of the images for the graphical abstract were obtained from https://smart.servier.com/. We acknowledge access to the facilities and expertise of the CIBM Center for Biomedical Imaging, a Swiss research center of excellence founded and supported by Lausanne University Hospital (CHUV), University of Lausanne (UNIL), Ecole Polytechnique Fédérale de Lausanne (EPFL), University of Geneva (UNIGE), and Geneva University Hospitals (HUG). This work was supported by the CONFIRM grant of the Hôpitaux Universitaires de Genève (HUG) Foundation (no. RC2-09) and the Swiss Multiple Sclerosis Society grant to D.M. and M.T.; the European Research Council (ERC) under the European Union's Horizon 2020 research and innovation program (ERC Consolidator grant agreement no. 815962) to M.T.; Swiss National Science Foundation (SNSF) grants to D.M. (310030_173010 and 310030_185321) and M.T. (310030_205042); and SNSF Professorship grants (PP00P3_144886 and PP00P3_172906) to M.T.

## AUTHOR CONTRIBUTIONS

M.S. set up and performed experiments, analyzed and interpreted data, and drafted figures and manuscript. K.S. set up and performed experiments and analyzed and interpreted data. N.H. and M.S. performed RNA sequencing analysis. D.R., N.S.-Z., M.-A.R., C.C., I.V., N.P., B.K., and O.S. helped with experiments. I.W. assisted in histological processing. M.G. assisted in setup of FACSymphony, and D.C. performed and analyzed FACSymphony. M.K. developed and applied computer-assisted image analysis algorithms. D.C. and O.B. performed the PET-CT. M.M. provided the MC-21 antibody. D.M. and M.T. conceptualized, designed, and supervised the project, interpreted data, and wrote the manuscript.

## DECLARATION OF INTERESTS

The authors declare no competing interests.

Received: August 28, 2020
Revised: July 24, 2021
Accepted: October 1, 2021
Published: October 22, 2021

## REFERENCES

Ajami, B., Bennett, J.L., Krieger, C., McNagny, K.M., and Rossi, F.M. (2011). Infiltrating monocytes trigger EAE progression, but do not contribute to the resident microglia pool. Nat. Neurosci. *14*, 1142–1149.

Allan, R.S., Waithman, J., Bedoui, S., Jones, C.M., Villadangos, J.A., Zhan, Y., Lew, A.M., Shortman, K., Heath, W.R., and Carbone, F.R. (2006). Migratory dendritic cells transfer antigen to a lymph node-resident dendritic cell population for efficient CTL priming. Immunity *25*, 153–162.

Buck, M.D., Sowell, R.T., Kaech, S.M., and Pearce, E.L. (2017). Metabolic instruction of immunity. Cell *169*, 570–586.

Cannon, B., and Nedergaard, J. (2004). Brown adipose tissue: function and physiological significance. Physiol. Rev. *84*, 277–359.

Chevalier, C., Stojanović, O., Colin, D.J., Suarez-Zamorano, N., Tarallo, V., Veyrat-Durebex, C., Rigo, D., Fabbiano, S., Stevanović, A., Hagemann, S., et al. (2015). Gut microbiota orchestrates energy homeostasis during cold. Cell *163*, 1360–1374.

Cignarella, F., Cantoni, C., Ghezzi, L., Salter, A., Dorsett, Y., Chen, L., Phillips, D., Weinstock, G.M., Fontana, L., Cross, A.H., et al. (2018). Intermittent fasting confers protection in CNS autoimmunity by altering the gut microbiota. Cell Metab. *27*, 1222–1235.e6.

Croxford, A.L., Lanzinger, M., Hartmann, F.J., Schreiner, B., Mair, F., Pelczar, P., Clausen, B.E., Jung, S., Greter, M., and Becher, B. (2015). The cytokine GM-CSF drives the inflammatory signature of CCR2+ monocytes and licenses autoimmunity. Immunity *43*, 502–514.

Davies, L.C., Rosas, M., Jenkins, S.J., Liao, C.T., Scurr, M.J., Brombacher, F., Fraser, D.J., Allen, J.E., Jones, S.A., and Taylor, P.R. (2013). Distinct bone marrow-derived and tissue-resident macrophage lineages proliferate at key stages during inflammation. Nat. Commun. *4*, 1886.

Demas, G., and Nelson, R. (2012). Ecoimmunology (Oxford University Press).

Dobin, A., Davis, C.A., Schlesinger, F., Drenkow, J., Zaleski, C., Jha, S., Batut, P., Chaisson, M., and Gingeras, T.R. (2013). STAR: ultrafast universal RNA-seq aligner. Bioinformatics *29*, 15–21.

Dranoff, G., Jaffee, E., Lazenby, A., Golumbek, P., Levitsky, H., Brose, K., Jackson, V., Hamada, H., Pardoll, D., and Mulligan, R.C. (1993). Vaccination with irradiated tumor cells engineered to secrete murine granulocyte-macrophage colony-stimulating factor stimulates potent, specific, and long-lasting anti-tumor immunity. Proc. Natl. Acad. Sci. USA *90*, 3539–3543.

Dunham-Snary, K.J., Sandel, M.W., Westbrook, D.G., and Ballinger, S.W. (2014). A method for assessing mitochondrial bioenergetics in whole white adipose tissues. Redox Biol. *2*, 656–660.

Fabbiano, S., Suárez-Zamorano, N., Rigo, D., Veyrat-Durebex, C., Stevanovic Dokic, A., Colin, D.J., and Trajkovski, M. (2016). Caloric restriction leads to browning of white adipose tissue through type 2 immune signaling. Cell Metab. *24*, 434–446.

Fabbiano, S., Suárez-Zamorano, N., Chevalier, C., Lazarević, V., Kieser, S., Rigo, D., Leo, S., Veyrat-Durebex, C., Gaïa, N., Maresca, M., et al. (2018).

Functional gut microbiota remodeling contributes to the caloric restriction-induced metabolic improvements. Cell Metab. *28*, 907–921.e7.

Fife, B.T., Huffnagle, G.B., Kuziel, W.A., and Karpus, W.J. (2000). CC chemokine receptor 2 is critical for induction of experimental autoimmune encephalomyelitis. J. Exp. Med. *192*, 899–905.

Foxman, E.F., Storer, J.A., Fitzgerald, M.E., Wasik, B.R., Hou, L., Zhao, H., Turner, P.E., Pyle, A.M., and Iwasaki, A. (2015). Temperature-dependent innate defense against the common cold virus limits viral replication at warm temperature in mouse airway cells. Proc. Natl. Acad. Sci. USA *112*, 827–832.

Ganeshan, K., Nikkanen, J., Man, K., Leong, Y.A., Sogawa, Y., Maschek, J.A., Van Ry, T., Chagwedera, D.N., Cox, J.E., and Chawla, A. (2019). Energetic trade-offs and hypometabolic states promote disease tolerance. Cell *177*, 399–413.e12.

Ganguly, D., Haak, S., Sisirak, V., and Reizis, B. (2013). The role of dendritic cells in autoimmunity. Nat. Rev. Immunol. *13*, 566–577.

Giladi, A., Wagner, L.K., Li, H., Dörr, D., Medaglia, C., Paul, F., Shemer, A., Jung, S., Yona, S., Mack, M., et al. (2020). Cxcl10$^{+}$ monocytes define a pathogenic subset in the central nervous system during autoimmune neuroinflammation. Nat. Immunol. *21*, 525–534.

Grant, R.W., and Dixit, V.D. (2015). Adipose tissue as an immunological organ. Obesity (Silver Spring) *23*, 512–518.

Guilliams, M., Mildner, A., and Yona, S. (2018). Developmental and functional heterogeneity of monocytes. Immunity *49*, 595–613.

Hansen, K.D., Gentry, J., Long, L., Gentleman, R., Falcon, S., Hahne, F., and Sarkar, D. (2021). Rgraphviz: Provides plotting capabilities for R graph objects (R package version 2.36.0).

Hasan, M., Seo, J.E., Rahaman, K.A., Kang, M.J., Jung, B.H., and Kwon, O.S. (2016). Increased levels of brain serotonin correlated with MMP-9 activity and IL-4 levels resulted in severe experimental autoimmune encephalomyelitis (EAE) in obese mice. Neuroscience *319*, 168–182.

Hettinger, J., Richards, D.M., Hansson, J., Barra, M.M., Joschko, A.C., Krijgsveld, J., and Feuerer, M. (2013). Origin of monocytes and macrophages in a committed progenitor. Nat. Immunol. *14*, 821–830.

Hotamisligil, G.S. (2017). Foundations of immunometabolism and implications for metabolic health and disease. Immunity *47*, 406–420.

Ikeda, K., Kang, Q., Yoneshiro, T., Camporez, J.P., Maki, H., Homma, M., Shinoda, K., Chen, Y., Lu, X., Maretich, P., et al. (2017). UCP1-independent signaling involving SERCA2b-mediated calcium cycling regulates beige fat thermogenesis and systemic glucose homeostasis. Nat. Med. *23*, 1454–1465.

Izikson, L., Klein, R.S., Charo, I.F., Weiner, H.L., and Luster, A.D. (2000). Resistance to experimental autoimmune encephalomyelitis in mice lacking the CC chemokine receptor (CCR)2. J. Exp. Med. *192*, 1075–1080.

Jaakkola, K., Saukkoriipi, A., Jokelainen, J., Juvonen, R., Kauppila, J., Vainio, O., Ziegler, T., Rönkkö, E., Jaakkola, J.J., and Ikäheimo, T.M.; KIAS-Study Group (2014). Decline in temperature and humidity increases the occurrence of influenza in cold climate. Environ. Health *13*, 22.

Jakubzick, C.V., Randolph, G.J., and Henson, P.M. (2017). Monocyte differentiation and antigen-presenting functions. Nat. Rev. Immunol. *17*, 349–362.

Jastroch, M. (2017). Uncoupling protein 1 controls reactive oxygen species in brown adipose tissue. Proc. Natl. Acad. Sci. USA *114*, 7744–7746.

Jordan, S., Tung, N., Casanova-Acebes, M., Chang, C., Cantoni, C., Zhang, D., Wirtz, T.H., Naik, S., Rose, S.A., Brocker, C.N., et al. (2019). Dietary intake regulates the circulating inflammatory monocyte pool. Cell *178*, 1102–1114.e17.

King, I.L., Dickendesher, T.L., and Segal, B.M. (2009). Circulating Ly-6C+ myeloid precursors migrate to the CNS and play a pathogenic role during autoimmune demyelinating disease. Blood *113*, 3190–3197.

Ko, H.J., Brady, J.L., Ryg-Cornejo, V., Hansen, D.S., Vremec, D., Shortman, K., Zhan, Y., and Lew, A.M. (2014). GM-CSF-responsive monocyte-derived dendritic cells are pivotal in Th17 pathogenesis. J. Immunol. *192*, 2202–2209.

Kohlgruber, A.C., LaMarche, N.M., and Lynch, L. (2016). Adipose tissue at the nexus of systemic and cellular immunometabolism. Semin. Immunol. *28*, 431–440.

Kox, M., van Eijk, L.T., Zwaag, J., van den Wildenberg, J., Sweep, F.C., van der Hoeven, J.G., and Pickkers, P. (2014). Voluntary activation of the sympathetic nervous system and attenuation of the innate immune response in humans. Proc. Natl. Acad. Sci. USA *111*, 7379–7384.

Li, C., Spallanzani, R.G., and Mathis, D. (2020). Visceral adipose tissue Tregs and the cells that nurture them. Immunol. Rev. *295*, 114–125.

Luo, Y., Chen, G.L., Hannemann, N., Ipseiz, N., Krönke, G., Bäuerle, T., Munos, L., Wirtz, S., Schett, G., and Bozec, A. (2015). Microbiota from obese mice regulate hematopoietic stem cell differentiation by altering the bone niche. Cell Metab. *22*, 886–894.

Man, K., Kutyavin, V.I., and Chawla, A. (2017). Tissue immunometabolism: development, physiology, and pathobiology. Cell Metab. *25*, 11–26.

McCarthy, D.J., Chen, Y., and Smyth, G.K. (2012). Differential expression analysis of multifactor RNA-seq experiments with respect to biological variation. Nucleic Acids Res. *40*, 4288–4297.

McDade, T.W. (2005). Life history, maintenance, and the early origins of immune function. Am. J. Hum. Biol. *17*, 81–94.

McInnes, L., Healy, J., and Melville, J. (2018). Umap: Uniform manifold approximation and projection for dimension reduction. arXiv, 1802.03426.

Menezes, S., Melandri, D., Anselmi, G., Perchet, T., Loschko, J., Dubrot, J., Patel, R., Gautier, E.L., Hugues, S., Longhi, M.P., et al. (2016). The heterogeneity of Ly6C$^{hi}$ monocytes controls their differentiation into iNOS$^{+}$ macrophages or monocyte-derived dendritic cells. Immunity *45*, 1205–1218.

Merad, M., Sathe, P., Helft, J., Miller, J., and Mortha, A. (2013). The dendritic cell lineage: ontogeny and function of dendritic cells and their subsets in the steady state and the inflamed setting. Annu. Rev. Immunol. *31*, 563–604.

Mildner, A., Mack, M., Schmidt, H., Brück, W., Djukic, M., Zabel, M.D., Hille, A., Priller, J., and Prinz, M. (2009). CCR2+Ly-6Chi monocytes are crucial for the effector phase of autoimmunity in the central nervous system. Brain *132*, 2487–2500.

Mufazalov, I.A., Schelmbauer, C., Regen, T., Kuschmann, J., Wanke, F., Gabriel, L.A., Hauptmann, J., Müller, W., Pinteaux, E., Kurschus, F.C., and Waisman, A. (2017). IL-1 signaling is critical for expansion but not generation of autoreactive GM-CSF+ Th17 cells. EMBO J. *36*, 102–115.

O'Neill, L.A., Kishton, R.J., and Rathmell, J. (2016). A guide to immunometabolism for immunologists. Nat. Rev. Immunol. *16*, 553–565.

Okin, D., and Medzhitov, R. (2012). Evolution of inflammatory diseases. Curr. Biol. *22*, R733–R740.

Page, N., Klimek, B., De Roo, M., Steinbach, K., Soldati, H., Lemeille, S., Wagner, I., Kreutzfeldt, M., Di Liberto, G., Vincenti, I., et al. (2018). Expression of the DNA-binding factor TOX promotes the encephalitogenic potential of microbe-induced autoreactive CD8$^{+}$ T cells. Immunity *48*, 937–950.e8.

Piccio, L., Stark, J.L., and Cross, A.H. (2008). Chronic calorie restriction attenuates experimental autoimmune encephalomyelitis. J. Leukoc. Biol. *84*, 940–948.

Platt, A.M., Rutkowski, J.M., Martel, C., Kuan, E.L., Ivanov, S., Swartz, M.A., and Randolph, G.J. (2013). Normal dendritic cell mobilization to lymph nodes under conditions of severe lymphatic hypoplasia. J. Immunol. *190*, 4608–4620.

Reynés, B., van Schothorst, E.M., Keijer, J., Palou, A., and Oliver, P. (2019). Effects of cold exposure revealed by global transcriptomic analysis in ferret peripheral blood mononuclear cells. Sci. Rep. *9*, 19985.

Roesler, A., and Kazak, L. (2020). UCP1-independent thermogenesis. Biochem. J. *477*, 709–725.

Ronchi, F., Basso, C., Preite, S., Reboldi, A., Baumjohann, D., Perlini, L., Lanzavecchia, A., and Sallusto, F. (2016). Experimental priming of encephalitogenic Th1/Th17 cells requires pertussis toxin-driven IL-1β production by myeloid cells. Nat. Commun. *7*, 11541.

Serbina, N.V., and Pamer, E.G. (2006). Monocyte emigration from bone marrow during bacterial infection requires signals mediated by chemokine receptor CCR2. Nat. Immunol. *7*, 311–317.

Stearns, S.C. (1992). The Evolution of Life Histories (Oxford University Press).

Steinman, R.M., and Banchereau, J. (2007). Taking dendritic cells into medicine. Nature *449*, 419–426.

Stojanović, O., Kieser, S., and Trajkovski, M. (2018). Common traits between the beige fat-inducing stimuli. Curr. Opin. Cell Biol. *55*, 67–73.

Timmermans, S., Bogie, J.F., Vanmierlo, T., Lütjohann, D., Stinissen, P., Hellings, N., and Hendriks, J.J. (2014). High fat diet exacerbates neuroinflammation in an animal model of multiple sclerosis by activation of the Renin Angiotensin system. J. Neuroimmune Pharmacol. *9*, 209–217.

Van Gassen, S., Callebaut, B., Van Helden, M.J., Lambrecht, B.N., Demeester, P., Dhaene, T., and Saeys, Y. (2015). FlowSOM: using self-organizing maps for visualization and interpretation of cytometry data. Cytometry A *87*, 636–645.

Wang, A., and Medzhitov, R. (2019). Counting calories: the cost of inflammation. Cell *177*, 223–224.

Wang, A., Luan, H.H., and Medzhitov, R. (2019). An evolutionary perspective on immunometabolism. Science *363*, eaar3932.

Weis, S., Carlos, A.R., Moita, M.R., Singh, S., Blankenhaus, B., Cardoso, S., Larsen, R., Rebelo, S., Schäuble, S., Del Barrio, L., et al. (2017). Metabolic adaptation establishes disease tolerance to sepsis. Cell *169*, 1263–1275.e14.

Winer, S., Paltser, G., Chan, Y., Tsui, H., Engleman, E., Winer, D., and Dosch, H.M. (2009). Obesity predisposes to Th17 bias. Eur. J. Immunol. *39*, 2629–2635.

Yu, G., and He, Q.Y. (2016). ReactomePA: an R/Bioconductor package for reactome pathway analysis and visualization. Mol. Biosyst. *12*, 477–479.

## STAR★METHODS

### KEY RESOURCES TABLE

| REAGENT or RESOURCE | SOURCE | IDENTIFIER |
|---|---|---|
| Antibodies | | |
| Anti-mouse HRP | DAKO | K4001; RRID:AB_2827819 |
| Anti-rabbit HRP | DAKO | K4003; RRID:AB_2630375 |
| Anti-rat HRP | Vectorlab | MP-7404-50; RRID:AB_2336531 |
| Armenian hamster anti-CD11c (clone N418) | BioLegend | 117328, 117308, 117343, 117309, 117312; RRID:AB_2129641, RRID:AB_313777, RRID:AB_2563099, RRID:AB_313778, RRID:AB_389328 |
| Armenian hamster anti-CD11c (clone N418) | eBioscience | 25-0114-82; RRID:AB_10372340 |
| Armenian hamster anti-CD3 (clone 145-2C11) | ThermoFisher, BioLegend | 11-0031-82, 100328, RRID:AB_464882, RRID:AB_893318 |
| Armenian Hamster anti-CD3 (clone 145-2C11) | BioLegend | 100314; RRID:AB_312679 |
| Armenian hamster anti-CD49a (clone Ha31/8) | BD | 564667; RRID:AB_2722549 |
| Mouse anti-APP A4 a.a. 66-81 (clone 22C11) | Sigma (formerly Millipore) | MAB348; RRID:AB_94882 |
| Mouse anti-CD64 (clone X54-5/7.1) | BioLegend | 139308, 139309; RRID:AB_2561963, RRID:AB_2562694 |
| Mouse anti-CX3CR1 (clone SA011F11) | BioLegend | 149013, 123135; RRID:AB_2565697, RRID:AB_2562622 |
| Mouse anti-NK1.1 (clone PK136) | BioLegend | 108727; RRID:AB_2132706 |
| Mouse anti-XCR1 (clone ZET) | BioLegend | 148207; RRID:AB_2564363 |
| Rabbit anti-CD3e (polyclonal) | DAKO | A0452; RRID:AB_2335677 |
| Rat anti-B220 (clone RA3-6B2) | BioLegend | 103207; RRID:AB_312992 |
| Rat anti-CCR2 (MC-21) | Provided by Matthias Mack | N/A |
| Rat anti-CD103 (clone M290) | BD | 564322; RRID:AB_2738744 |
| Rat anti-CD107b (Mac3) (clone M3/84) | BioLegend | 108502; RRID:AB_313383 |
| Rat anti-CD115 (clone AFS98) | BioLegend | 135505, 135515, 135523; RRID:AB_1937254, RRID:AB_2562679, RRID:AB_2566459 |
| Rat anti-CD117 (clone ACK2, 2B8) | BioLegend | 135111, 105827; RRID:AB_2131136, RRID:AB_10898120 |
| Rat anti-CD11b (clone M1/70) | BioLegend | 101242, 101228, 101222, 101263; RRID:AB_2563310, RRID:AB_893232, RRID:AB_493705, RRID:AB_2629529 |
| Rat anti-CD11b (clone M1/70) | BD | 553310; RRID:AB_394774 |
| Rat anti-CD127 (clone A7R34) | BioLegend | 135009; RRID:AB_1937252 |
| Rat anti-CD135 (clone A2F10) | BioLegend | 135310; RRID:AB_2107050 |
| Rat anti-CD16/32 TruStain FcX (clone 93) | BioLegend | 101320; RRID:AB_1574975 |
| Rat anti-CD19 (clone 6D5) | BioLegend | 115534; RRID:AB_2072925 |
| Rat anti-CD4 (clone GK1.5) | BioLegend | 100422; RRID:AB_312707 |
| Rat anti-CD45 (clone 30-F11) | BioLegend | 103114, 103108; RRID:AB_312979, RRID:AB_312973 |
| Rat anti-CD8 (clone 53-6.7) | BD | 563786; RRID:AB_2732919 |
| Rat anti-F4/80 (clone BM8) | BioLegend | 123114; RRID:AB_893478 |
| Rat anti-F4/80 (clone BM8) | BioLegend | 107622, RRID:AB_493727 |
| Rat anti-GM-CSF (clone MP1-22E9) | ThermoFisher | 11733181; RRID:AB_465420 |

(*Continued on next page*)

*Continued*

| REAGENT or RESOURCE | SOURCE | IDENTIFIER |
|---|---|---|
| Rat anti-IFNg (clone XMG1.2) | BioLegend | 508510, 505830; N/A, RRID:AB_2563105 |
| Rat anti-IFNg (XMG1.2) | Bio X Cell | BE0055; RRID:AB_1107694 |
| Rat anti-IL-17 (clone TC11-18H10.1) | BioLegend | 506904; RRID:AB_315464 |
| Rat anti-Ly6C (clone HK1.4) | BioLegend | 128036, 128037; RRID:AB_2562353; RRID:AB_2562630 |
| Rat anti-Ly6G (clone 1A8) | BioLegend | 127622, 126615, 565707; RRID:AB_10643269, RRID:AB_2562776, N/A |
| Rat anti-MHCII (clone M5/114.15.2) | BioLegend | 107620, 107606, 107631, 107622; RRID:AB_493527, RRID:AB_313321, RRID:AB_10900075, RRID:AB_493727 |
| Rat anti-mouse CD49d (clone R1-2) | BioLegend | 149027; RRID:AB_2565937 |
| Rat anti-NOS2 (clone CXNFT) | ThermoFisher | 53-5920-82; RRID:AB_2574423 |
| Rat anti-PDCA-1 (clone 927) | BioLegend | 127012; RRID:AB_1953287 |
| Rat anti-Sca1 (clone D7) | BioLegend | 108116; RRID:AB_493269 |
| Rat anti-Siglec-F (clone E50-2440) | BD | 552126; RRID:AB_394341 |
| Rat anti-Ter119 (clone Ter119) | BioLegend | 116228; RRID:AB_893636 |
| Rat IgG2b isotype | Bio X Cell | BE0090; RRID:AB_1107780 |
| Sheep anti-Arg1 | R&D | IC5868P |
| Syrian Hamster anti-CD28 (clone 37.51) | BioLegend | 102112; RRID:AB_312877 |
| **Chemicals, peptides, recombinant proteins** | | |
| 2-Mercaptoethanol | Biorad | 1610710 |
| Acetone | Sigma | 179124 |
| Brefeldin A | BioLegend | 420601 |
| CL316,243 | Sigma | C5976 |
| Collagenase A | Roche | 11088882001 |
| Collagenase D | Sigma | 11088866001 |
| DAB | DAKO | K5001 |
| DAPI | ThermoFisher | D1306 |
| Dibutyl phthalate,99% | Sigma | 524980 |
| DMEM | ThermoFisher | 41965-039 |
| DNase | Roche | 10104159001 |
| FA Folic Acid solution | Sigma | F8758 |
| Fluorescein isothiocyanate isomer I | Sigma | F7250 |
| Hemalun | Merck | 1092490.500 |
| Heparin | Sigma | H3393 |
| hTGF-beta | Peprotech | 100-21C |
| IL-12 | Peprotech | 210-12 |
| IL-18 | MBL (Biozol) | B004-5 |
| IL-2 | ebioscience | 34-8021-82 |
| IL-23 | Miltenyi | 130-096-676 |
| IL-6 | Peprotech | 216-16 |
| IL-7 | Peprotech | 217-17 |
| Ionomycin | Sigma | IO634 |
| L-Arginine | Sigma | 11009 |
| L-Asparagine | Sigma | A0884 |
| L-Glutamin | Bioconcept | 5-10K00H |
| Lithium Carbonate | Merck | 5671.0250 |
| Luxol Fast Blue | BDH laboratories | 340443P |
| Monensin | BioLegend | 420701 |

(*Continued on next page*)

*Continued*

| REAGENT or RESOURCE | SOURCE | IDENTIFIER |
|---|---|---|
| NEAA 100x | GIBCO | 11140-035 |
| Penicilin-Streptomycin solution | AMIMED | 4-01F-00H |
| Percoll | GE Healthcare | 17-0891-01 |
| Periodoc Acid | Merck | 1005240100 |
| PMA | Sigma | P1585 |
| Schiff's reagent | Merck | 1.09033.0500 |
| Sodium Pyruvate | Sigma | S8636 |
| Thioglycollate medium | Sigma | T9032 |
| VIT Vitamin mix solution | Sigma | M6985 |
| **Critical commercial assays** | | |
| AccuCheck Counting Beads | Molecular Probes | PCB100 |
| BD FACS Lysing Solution | BD | 349202 |
| CD4(l3t4) microbeads mouse | Miltenyi | 130-117-043 |
| cDNA Reverse Transcription Kit | Applied Biosystems | 4368814 |
| Fixation buffer | BioLegend | 420801 |
| FoxP3/Transcription Factor Staining Buffer Set | eBioscience | 00-5523-00 |
| heat inactivated mycobacterium tuberculosis H3/RA | BD Difco | 231141 |
| Incomplete Freund's adjuvant | BD Difco | 263910 |
| Intracellular Staining Perm Wash Buffer | BioLegend | 421002 |
| MOG peptide 35-55 | Peptides&elephants | N/A |
| Nextera kit | Illumina | N/A |
| Pertussis toxin | Sigma/ Calbiochem | P7208/ 516560 |
| RBC Lysis buffer | BioLegend | 420301 |
| RNAlater stabilization solution | ThermoFisher | AM7020 |
| RNeasy plus Micro Kit | QIAGEN | 74034 |
| RNeasy plus Mini Kit | QIAGEN | 74134 |
| PowerUp SYBR Green Master Mix | Applied Biosystems | A25741 |
| SMART-Seq v4 ultra-low input kit | Clontech | N/A |
| TRIzol reagent | ThermoFisher | 15596026 |
| TruSeq stranded mRNA kit | Illumina | N/A |
| Versacomp beads | Beckman Coulter | B22804 |
| Zombie NIR Fixable Viability Kit | BioLegend | 423105 |
| **Deposited data** | | |
| RNA sequencing data | This paper | GEO: GSE172021 |
| RNA sequencing data | This paper | GEO: GSE183321 |
| **Experimental models: Cell lines** | | |
| B16-GMCSF cells | Dranoff et al., 1993 | N/A |
| **Experimental models: Organisms/strains** | | |
| Mouse: 2D2 | The Jackson Laboratory | 006912 |
| Mouse: C57BL/6 | Charles River, Janvier | N/A |
| Mouse: Ccr2-KO | The Jackson Laboratory | 004999 |
| Mouse: Ucp1-KO | The Jackson Laboratory | 003124 |
| **Oligonucleotides** | | |
| M. musculus Ucp1 | 5′-GGCCTCTACGACTCAGTCCA-3′ | 5′-TAAGCCGGCTGAGATCTTGT-3′ |
| M. musculus Cidea | 5′-TGCTCTTCTGTATCGCCCAGT-3′ | 5′-GCCGTGTTAAGGAATCTGCTG-3′ |
| M. musculus Ppargc1a | 5′-AAGTGTGGAACTCTCTGGAACTG-3′ | 5′-GGGTTATCTTGGTTGGCTTTATG-3′ |
| M. musculus Ppara | 5′-AGAGCCCCATCTGTCCTCTC-3′ | 5′-ACTGGTAGTCTGCAAAACCAAA-3′ |

(*Continued on next page*)

*Continued*

| REAGENT or RESOURCE | SOURCE | IDENTIFIER |
|---|---|---|
| M. musculus Pparg | 5′-AGGCGAGGGCGATCTTGACAG-3′ | 5′-AATTCGGATGGCCACCTCTTTG-3′ |
| M. musculus Prdm16 | 5′-CAGCACGGTGAAGCCATT-3′ | 5′-GCGTGCATCCGCTTGTG-3′ |
| M. musculus 36B4 | 5′- GTACCCATTGATGATGGAGTGT-3′ | 5′-TGAAGTGCTCGACATCACAG-3′ |
| M. musculus B2m | 5′-TTGTCTCACTGACCGGCCT-3′ | 5′-TATGTTCGGCTTCCCATTCTCC-3′ |
| Software and Algorithms | | |
| FastQC v.0.11.5 | Babraham bioinformatics | https://www.bioinformatics.babraham.ac.uk/projects/fastqc/ |
| FLIR Tools+ software | FLIR technologies | https://www.flir.com/products/flir-tools/ |
| FlowJo 10.2 | TreeStar | https://www.flowjo.com/solutions/flowjo/downloads/previous-versions |
| GraphPad 8 | Prism | https://www.graphpad.com/scientific-software/prism/ |
| HTSeq v0.9.1 | HTSeq | https://htseq.readthedocs.io/en/master/ |
| MetaCore | Clarivate Analytics | https://clarivate.com/cortellis/wp-content/uploads/sites/4/2020/02/MetaCore.pdf |
| Pannoramic Viewer software | 3DHistech | https://www.3dhistech.com/research/software-downloads/ |
| Picard tools v.1.141 | N/A | https://broadinstitute.github.io/picard/ |
| QuPath v0.2.2 | QuPath | https://qupath.github.io/QuPath-v0.2.0.html |
| R language and environment for statistical computing and graphics | N/A | https://www.r-project.org |
| R/Bioconductor package EdgeR v. 3.4.2 | (McCarthy et al., 2012) | https://bioconductor.org/packages/release/bioc/html/ReactomePA.html |
| R/Bioconductor package topGO | N/A | https://bioconductor.org/packages/release/bioc/vignettes/topGO/inst/doc/topGO.pdf |
| ReactomePA R-package | (Yu and He, 2016) | https://bioconductor.org/packages/release/bioc/html/ReactomePA.html |
| Rgraphviz | (Hansen et al., 2021) | https://www.bioconductor.org/packages/release/bioc/html/Rgraphviz.html |
| STAR aligner v.2.6.0c | (Dobin et al., 2013) | N/A |
| Seahorse Wave Desktop Software | Agilent | N/A |
| VivoQuant v.2020-build9 | inviCRO | http://www.vivoquant.com/ |
| Other | | |
| Attune NxT | ThermoFisher | N/A |
| AutoMACS Pro | Miltenyi | N/A |
| AxioScan Z1 | Zeiss | N/A |
| Bioanalyzer Agilent 2100 | Agilent | https://www.agilent.com/en/product/automated-electrophoresis/bioanalyzer-systems/bioanalyzer-instrument/2100-bioanalyzer-instrument-228250 |
| BD FACSAria II | BD Biosciences | N/A |
| BD FACSymphony | BD Biosciences | N/A |
| BD LSRFortessa | BD Biosciences | N/A |
| TProfessional Basic Thermocycler | Biometra | N/A |
| Bio-Rad S3 | Bio-Rad | N/A |
| FLIR E60 thermal camera | FLIR systems | N/A |
| HiSeq 4000 | Illumina | N/A |
| Light Cycler 480-II | Roche | N/A |
| MoFlo Astrios | Beckman Coulter | N/A |
| NanoDrop | ThermoFisher | N/A |
| Pannoramic 250 FLASH II | 3Dhistech | N/A |
| Seahorse XF24 Analyzer | Agilent | N/A |
| Tissue Lyser II | QIAGEN | N/A |
| Triumph PET/SPECT/CT | TriFoil Imaging | N/A |

## RESOURCE AVAILABILITY

### Lead contact

Further information and requests for resources and reagents should be directed to and will be fulfilled by the lead contact, Mirko Trajkovski (mirko.trajkovskiunige.ch).

### Materials Availability

This study did not generate new unique reagents.

### Data and Code Availability

- All sequencing data generated in this study are deposited at NCBI Gene Expression Omnibus (GEO) repository with accession numbers GSE172021 and GSE183321, and are publicly available as of the date of publications. Microscopy data reported in this paper will be shared by the lead contact upon request.
- The scripts used for the RNaseq data analysis and generating figures are available at https://github.com/Nhadadi/EAE_mouse_RNaseqAnalysis_multiTissue
- Any additional information required to reanalyze the data reported in this paper is available from the lead contact upon request.

## EXPERIMENTAL MODEL AND SUBJECT DETAILS

### Mice

Male 8 weeks old C57BL/6J mice were obtained from Charles River, or Janvier (France). *Ucp1*-KO (The Jackson Laboratory), their littermate controls, *Ccr2*-KO (The Jackson Laboratory) and 2D2 (The Jackson Laboratory) mice were bred in house at room temperature (RT) of 22°C. All mice were on C57BL/6 genetic background. Experiments were started following one week of acclimatation of the purchased mice, or on 9 weeks old mice for the in house bred colonies. Mice were housed in a specific pathogen free (SPF) facility in 12 h day/night cycles at RT, fed irradiated standard chow diet (RM3 from Special Diets Service (SDS, product code 801066); or SAFE R150 diet from SAFE, https://safe-lab.com/safe-wAssets/docs/product-data-sheets/diets/safe_150_ds.pdf), given autoclaved water from bottles, and inspected daily by the responsible animal caretakers at the University of Geneva in addition to the specified measurements and interventions done by the experimenters. Cold exposure was applied in a light- and humidity-controlled climatic chamber (TSE, Germany) under SPF conditions, at 10°C for 2 weeks before immunization with an additional initial acclimatization period of 5 days at 18°C and 5 days at 14°C, as well as during EAE. Warm exposure of 34°C was applied for 7 days before immunization, and during EAE. All climate chamber experiments were performed with 2 mice per cage without bedding and nesting material for enrichment to ensure controlled temperature conditions. CL316,243 (Sigma) was i.p. injected daily 7 days before immunization and until sacrifice. Body temperature was determined with infrared camera FLIR E60 (FLIR, UK) taking the mean temperature of both eyes using the FLIR Tools+ software. All animal experiments were performed at the University of Geneva with authorization by the responsible Geneva cantonal and Swiss federal authorities for animal experimentation and in accordance with the Swiss law for animal protection.

## METHOD DETAILS

### EAE induction and scoring

For active EAE immunization, complete Freund's adjuvant was prepared by mixing 10mg/mL heat inactivated mycobacterium tuberculosis H3/RA (Difco) with incomplete Freund's adjuvant (Difco). To create an emulsion, this was mixed 1:1 with MOG peptide 35-55 (4 mg/mL, peptides & elephants). Mice were anesthetized and 50 ul of the emulsion was injected into the left and right flank each (200 ug peptide/mouse), followed by i.v. injection of 300 or 400 ng pertussis toxin (Sigma or Calbiochem). After two days, mice received additional 300 or 400 ng pertussis toxin i.p.

For Th1 adoptive transfer EAE, splenocytes of 2D2 T cell receptor transgenic mice were cultured for 2 days with MOG35-55 peptide (20 μg/mL), IL-2 (5 ng/mL, ebioscience) and IL-7 (5 ng/mL, Peprotech), 4 days with IL-2 (5 ng/mL) and IL-7 (5 ng/mL) and 1 day with anti-CD3/28 (0.5 ng/ul, Biolegend), IL-12 (20 ng/mL, Peprotech) and IL-18 (25 ng/mL, MBL (Biozol)) at 37°C. Per mouse, 1-2 million cells were transferred (i.p.) and animals were injected with 67 ng pertussis toxin on day 0 (i.v.) and day 2 (i.p.) of EAE. Congenic animals (CD45.1 and CD45.2) were used to later distinguish endogenous and transferred T cells.

For Th17 adoptive transfer EAE, wildtype donor mice were actively immunized as described above and after 7 days their splenocytes lysed, cultured together with cells from dLNs for 3 days with IL-6 (5 ng/mL, Peprotech), hTGF-beta (0.25 ng/mL, Peprotech), anti-IFNg (14 ug/mL, Bio X Cell), IL-23 (6.5 ng/mL, Miltenyi) and MOG peptide (35 ug/mL) and sorted via positive selection of $CD4^+$ T cells (MACS, Miltenyi). Per recipient, 3 million $CD4^+$ T cells were transferred by iv. injection and animals were injected i.p. with pertussis toxin on day 0 and day 2 of EAE (300 ng).

Starting at the disease onset, approx. 8-10 days after induction of EAE, disease severity was monitored using an established scale from 0 to 4 to describe clinical symptoms: 0, no detectable signs of classical EAE; 0.5, paresis of distal limb tail; 1.0, tail paralysis; 1.5, hind-limb weakness; 2, hind-limb paresis; 2.5, partial hind-limb paralysis; 3, complete bilateral hind-limb paralysis; 3.5, ascending paralysis to torso; 4, paralysis of forelimbs and hind limbs. Blinding was not possible for EAE scoring since the cold-, or the

warm-exposed mice were kept in the climate chambers under cold or warm temperatures respectively, and cages were accordingly temperature-acclimatized once taken out for scoring. Mice with scores > 3.5 were sacrificed. Dead animals were excluded or in warm exposure experiment given a score of 5 on death day due to increased deaths and high scores. Animals that reached a score > 1.5 were provided with their chow diet, watered, inside the cage.

### B16-GMCSF tumor and thioglycolate elicited peritoneal inflammation

GMCSF-expressing B16 melanoma tumor cells (Dranoff et al., 1993) were cultured and s.c. engrafted as described (Menezes et al., 2016) into cold exposed and room temperature mice. In brief, 1.5 × 105 to 3 × 105 cells in 50 μL of PBS were injected subcutaneously close to the right shoulder. Blood was drawn on several days after tumor implantation in heparin (Sigma) to analyze circulating monocyte expansion and phenotype using flow cytometry. For peritoneal inflammation, cold-exposed and room temperature mice were i.p. injected with 1ml of 4% thioglycolate (Sigma), as described before (Davies et al., 2013). Animals were sacrificed after 24 h for analysis of peritoneal monocytes and monocyte derived cells using flow cytometry.

### FITC migration of DCs using skin painting of the flank

Mice were anesthetized with isoflourane, a small area of one flank (about 1x1cm) was shaved and 20 ul of FITC solution was applied, consisting of 1% FITC (Sigma-Aldrich: Fluorescein isothiocyanate isomer I) in Aceton/Dibutylphthalate (1:1, Sigma). After 12 h and 18 h, the 3 draining lymph nodes (axillary, brachial and inguinal) of ipsi- and contralateral side were harvested and cells harvested as described above.

### Antibody treatment for CCR2$^{+}$ monocyte depletion

Monocytes were depleted by daily i.p. injections of anti-CCR2 mAb (clone: MC-21; 40 μg), starting one day before immunization on 8 consecutive days until sacrifice. Control mice received isotype rat IgG2b (Bio X Cell) at the same dose. Depletion efficiency was tested 2 days before EAE onset and sacrifice.

### Positron emission tomography – computer tomography (PET-CT)

Mice cold exposed for 2 weeks and additional 5 days after immunization, were anesthetized with 2% isoflurane and were injected in the venous sinus with 5–6 megabecquerel (MBq) [$^{18}$F]FDG. Mice were then left awake at RT during the uptake time of 20 min. Then 10 min prior to PET scan, mice were subjected to CT scans in a Triumph microPET/SPECT/CT system (TriFoil). Images were obtained at 80 peak kilovoltage (kVp) and 160 μA, and 1'024 projections were acquired during the 360° rotation with a field of view of 71.3 mm (1.7 × magnification). After 20 min of [$^{18}$F]FDG uptake, PET scans were started for a total duration of 10 min.

PET scans were reconstructed with the built-in LabPET software using an OSEM3D (20 iterations) algorithm, and images were calibrated in Bq per milliliter by scanning a phantom cylinder. The Triumph XO software, which uses a back-projection engine, was used to reconstruct the CT scans with a matrix of 512 and a voxel size of 0.135 mm. The VivoQuantTM software version 2020-build9 (inviCRO, Boston MA) was used to co-register the CT and PET scans and to quantitatively analyze the datasets and generate pictures. Indicated adipose-tissues volumetric and density analysis was conducted using signal-intensity thresholds to create regions of interest (ROIs) on CT scans. Then, PET series were converted to display standardized uptake values (SUVs) adjusted to the body weight of the animals and merged with the CT sets. 3D ROIs derived from CT scans were used to quantify the uptake of [$^{18}$F]FDG in the indicated adipose tissues and muscle. In order to measure the volume of activated interscapular BAT, a 3D ROI was first delineated visually by contouring the [$^{18}$F]FDG activity. A new ROI was then derived based on a threshold equal to the mean [$^{18}$F]FDG minus one standard deviation of all voxels within the primary defined ROI. This final volume was used to report the activated BAT.

### Histology

For histologic analyses of spinal cord, mice were kept until 1-2 days after peak, perfused with PBS and subsequently 4% paraformaldehyde (PFA) and additionally immersion fixed in 4% PFA. Sectioning, embedding and staining were performed as previously described (Page et al., 2018). In brief, brains and spinal cords were prepared and fixed in 4% paraformaldehyde (PFA) and embedded in paraffin. Antigen retrieval was performed according to standardized protocols by heating with citrate buffer (pH6). Endogenous peroxidases (peroxidase blocking reagent, Dako) were neutralized and unspecific binding blocked for 5 min (PBS/1% BSA/2% FCS). Tissue 3μm sections were either stained for LFB/PAS (myelin) or incubated with rat anti-CD3 (CD3-12, Biorad). Bound primary antibodies were visualized with biotin-labeled anti-rat antibody and streptavidin-peroxidase staining method using polymerized 3,30-diamino- benzidine (all reagents from Dako; haemalaun counterstaining of nuclei). Mice shown for histologic evaluation were control mice of an experiment and therefore injected with diphtheria toxin (Sigma). Stainings were developed with DAB (DAKO) and nuclei counterstained with hemalum (Merck). Sections were scanned using Pannoramic Digital Slide Scanner 250 FLASH II (3DHISTECH). Quantifications were performed blinded to the experimental condition. Anti-CD3 (polyclonal, DAKO) and anti-mac3 (M3/84, Biolegend) stainings were automatically quantified using Definiens Developer software with a custom-made script. Quantifications of Luxol Fast Blue (BDH laboratories)-Perdiodic Acid (Merck)-Schiff's (Merck) (LFB-Pas) lesion areas, anti-APP (22C11, Millipore) and lesion number were performed manually using Pannoramic Viewer software (3DHISTECH). Number of lesions were counted in APP

staining and only lesions were taken into account that were found in LFB-Pas as well. APP was quantified within lesions marked in LFB-Pas staining and reported per total white matter area. For representative LFB-Pas images, contrast was equally adjusted in the compared conditions in Adobe Photoshop.

For histologic analyses of adipose tissues, tissues were fixed in 4% paraformaldehyde (Sigma-Aldrich), paraffin embedded, cut in sections (5 μm) and stained with hematoxylin-eosin (H&E). Images were acquired using AxioScan Z1 (Zeiss) and the cell/lipid droplet size quantified with Qupath software (V0.2.2) using machine-learning classifiers.

### Immune cell isolation from tissues

Peripheral blood samples (10-30 μl) were obtained by facial vein puncture in 1 μl heparin (10U/μl, Sigma). Blood erythrocytes were lysed and cells fixed using BD FACS Lysing Solution. For other tissues that required red blood cell lysis, RBC Lysis buffer (Biolegend) was used. For the isolation of immune cells from the CNS, mice were anesthetized and transcardially perfused with PBS. Brain and spinal cord were minced, digested in DMEM (ThermoFisher) with Collagenase A (1mg/mL, Sigma) and DNaseI (0.1 mg/mL, Roche) for 1 h at 37°C and homogenized using 70-μm cell strainers (BD). Leukocytes were separated using a discontinuous Percoll (GE healthcare) gradient (30% / 70%, 2500 RPM, 30 min, 4°C). Bone marrow cells were flushed from 1 femur per mouse. For analysis of DC and monocyte populations, axillary and brachial lymph nodes or spleen were cut into small pieces and digested in DMEM with collagenase D (1mg/mL, Roche) and DNaseI (10μg/mL, Roche) for 30-35 min at 37°C under constant pipetting. For studies of all other immune cells, lymph nodes or spleens were mashed through a 70 μm cell strainer. For splenocytes, red blood cell lysis was performed (BioLegend).

### Flow cytometry

Dead cells were excluded from the analysis using Zombie NIR or Aqua Fixable Viability kit (BioLegend) for all tissues except blood. Surface staining was performed with directly labeled antibodies in FACS buffer (DPBS, 2.5% FCS, 10mM EDTA). Compensation controls were set up using Versacomp beads (Beckman Coulter). Antibodies were from BioLegend if not stated otherwise. For staining of bone marrow progenitors and mature monocytes, the following antibodies were used: Lin (CD3 (145-2C11), CD19 (6D5), NK1.1 (PK136), Ly6G (1A8), Ter-119), CD127 (A7R34), CD117 (ACK2, 2B8), CD115 (AFS98), CD135 (A2F10), Ly6C (HK1.4), CD11b (M1/70), Sca1 (D7), CD11c (N418), MHCII (M5/114.15.2). In figures, monocytes and monocyte-derived cells were abbreviated as "M" for simplicity reasons. Both Ly6C$^{hi}$ monocytes and monocyte derived cells were defined mainly by their Ly6C expression (in addition to and exclusion of other markers), but irrespective of a co-expression of CD11c or pro/anti-inflammatory cytokines. "M" therefore comprises both, undifferentiated Ly6C$^{hi}$ monocytes and monocytes that already gained APC or macrophage like functions but still express Ly6C. For characterization of blood and bone marrow monocytes, the following antibodies were used: CD45 (30-F11), Ly6G, CD11b, CD115, Ly6C, MHCII. For characterization of T cells in various tissues, the following antibodies were used: CD45, CD11b, Ly6G, CD4 (GK1.5), CD3, CD8 (53-6.7, BD), GM-CSF (MP1-22E9, ThermoFisher), IL-17 (TC11-18H10.1), IFNg (XMG1.2). Unspecific binding to FC receptors was blocked using anti-CD16/32 (BioLegend). Intracellular stainings were performed according to manufacturer's instructions: Fixation/Intracellular Staining Permeabilization Wash Buffer (BioLegend) and Fixation buffer (BioLegend) were used for Arg1 (IC5868P, R&D), iNOS (CXNFT), IL-17, IFNg and GM-CSF. To assess for intracellular cytokine production of T cells, leukocytes were cultured for 4 h in the presence of PMA (end 50ng/mL, Sigma) and Ionomycin (end 1μg/mL) (Sigma), monensin (1:1000, BioLegend), and brefeldin A (1:1000, BioLegend). Absolute cell numbers were quantified using AccuCheck Counting Beads (Invitrogen). Flow cytometric samples were acquired on an Attune NxT (ThermoFisher) or LSRFortessa (BD) flow cytometer using compensation controls. FlowJo software (Treestar, Version 10) was used for analysis. Further antibodies used in DC analysis or high dimensional analysis, that were not yet mentioned before are CD49a (Ha31/8, BD), CD64 (X54-5/7.1), CX3CR1 (SA011F11), XCR1 (ZET), B220 (RA3-6B2), CD103 (M290, BD), F4/80 (BM8), CD49d (R1-2), PDCA-1 (927), Siglec-F (E50-2440, BD). High-dimensional flow cytometry analysis was performed using BD FACSymphony. Raw data was pre-processed using FlowJo followed by transformation, percentile normalization in R, dimensionality reduction and visualization by Uniform Manifold Approximation and Projection (UMAP) (McInnes et al., 2018). The FlowSOM algorithm was used for automated clustering (Van Gassen et al., 2015) using UMAP with overlaid mean marker expression values and a heatmap of median expression values. Data shown in Figure 2C is the same as in Figure 5E but was visualized together with data from other time points to highlight shifts of populations over the time in Figure 5E.

### Oxygen Consumption Rate (OCR)

OCR was determined as before (Dunham-Snary et al., 2014; Fabbiano et al., 2016, 2018), in 3.2-8mg punches (2.5 mm) of adipose tissue. After washing in wash buffer (25mM HEPES, 1% fatty acid-free BSA, 2.5 mM glucose, in salt solution: 4mM KCl, 115 mM NaCl, 1 mM MgCl2, 1.5 mM KH2PO4, 2 mM MgSO4, 1.5 mM CaCl2 at pH 7.4), tissue punches were placed in islet capture plates (model XF24, Seahorse Bioscience) and washed with wash and subsequently with respiration buffer (0.1% fatty acid-free BSA, 10 mM glucose, 2 mM L-glutamine, 0.5 mM L-carnitine, 1 mM sodium pyruvate in salt solution at pH 7.4), in which they were further equilibrated for 50 or 60 min at 37°C. Samples were analyzed using a Seahorse XF24 Analyzer (Seahorse Bioscience) and Wave software with 3 min mix; 2 min rest; 3 min measurements in basal condition.

### RNA extraction for RNA sequencing and qPCR

After preparation from mice, spinal cord and adipose tissues were stored at −80°C until further processed. For RNA isolation, frozen tissues were mechanically homogenized in 1 mL Trizol (Thermo Fisher Scientific) with 1 stainless steel bead (5 mm) per sample using

the TissueLyserII (QIAGEN) by shaking for 50 s at 30 Hz. 200 μL chloroform was added to homogenized samples in trizol, followed by shaking for 15 s and centrifugation (15 min, 12000 RCF, 4°C). The chloroform phase was collected, shaken for 15 s with 500 μL isopropanol and centrifuged (15 min, 12000 RCF, 4°C). The pellet obtained was washed twice with 70% ethanol (10 min, 8000 RCF, 4°C) and resuspended in 50 μL PCR-grade water. Bone marrows were flushed right after sectioning from mouse, cells centrifuged, loaded onto shredder columns (QIAGEN). Shredded bone marrow cells or FACS sorted cells were frozen (−80°C) in RLT buffer with 1% beta-mercaptoethanol until RNA extraction via RNA mini kit or micro kit (QIAGEN), respectively. For Sequencing, RNA integrity number (RIN) was determined (Bioanalyzer 2100, Agilent). For qPCR, RNA concentration and purity were determined (NanoDrop, Thermo Fisher Scientific) and 1 μg RNA was used per sample for retrotranscription using the High-Capacity cDNA Reverse Transcription Kit (Applied Biosystems). Expression of mRNA was measured by qPCR on a LightCycler 480 II (Roche) with PowerUp SYBR Green Master Mix (Applied Biosystems). Relative mRNA expression was normalized to at least two house keeping genes and to room temperature control mice.

### Blood monocyte purification for RNA sequencing

Blood was taken retro-orbital under terminal anesthesia in polypropylen facs tubes containing 7μl heparin (10U/μl) and coated with 100 IU/mL heparin. Anti-CD115-PE was directly added, and MACS separation was performed using Anti-PE MicroBeads (Miltenyi) and AutoMACS Pro Seperator (Miltenyi). Immediately after, monocytes were sorted as CD115+, DAPI- (ThermoFisher) cells (FACSAriaII, BD, Bio-Rad S3 or MoFlo Astrios, Beckman Coulter).

### RNaseq sequencing and analysis

mRNA sequencing was performed at the iGE3 Genomics Platform at the CMU of the University of Geneva. Libraries for sequencing were prepared with the TruSeq stranded mRNA kit (Illumina) for bone marrow and spinal cord. The SMART-Seq v4 ultra-low input kit (Clontech) combined with the Nextera kit (Illumina) were used respectively for cDNA amplification and library preparation for monocytes (steady state and EAE). Bone marrow, spinal cord, and monocytes (EAE) were sequenced with read length SR50 and steady state monocytes with read length SR100 (Illumina HiSeq 4000). The sequencing quality control was done with FastQC v.0.11.5 (https://www.bioinformatics.babraham.ac.uk/projects/fastqc/). The reads were mapped with STAR aligner (Dobin et al., 2013) to the UCSC *Mus musculus* mm10 reference. The transcriptome metrics were evaluated with the Picard tools v.1.141 (https://picard.sourceforge.net/). The table of counts with the number of reads mapping to each gene feature of the *Mus musculus* mm10 reference was prepared with HTSeq v0.9.1 (htseq-count, https://www.huber.embl.de/users/anders/HTSeq/). Raw counts were then further processed and analyzed by R/Bioconductor package EdgeR v. 3.4.2 (McCarthy et al., 2012), for differential expression analysis. The counts were normalized according to the library size and filtered. Only genes having log count per million reads (cpm)>0 were kept for further analyses. After normalization of the counts, transcript abundances were compared in pairwise conditions in a modified Fischer exact test (as implemented in edgeR). The differentially expressed genes p values were corrected for multiple testing error with a 5% FDR (false discovery rate). The correction used is Benjamini-Hochberg (BH). Transcripts with log(cpm)>0 and $p \leq 0.05$ were subsequently subjected to pathway analysis. For the relativeness and reactome analysis, genes were called significantly differentially expressed between any given two conditions when $p < 0.05$ and $FC > 2$. Reactome pathways database was used with ReactomePA R-package (Yu and He, 2016), reporting the enrichment ratio (# DEGs/Total Genes in the dataset) and FDR-adjusted P value computed by Fisher exact test. For gene ontology analysis, R/Bioconductor package topGO (https://bioconductor.org/packages/release/bioc/vignettes/topGO/inst/doc/topGO.pdf), together with Rgraphviz was used. MetaCore (Clarivate Analytics) Pathway Maps, Gene Ontology and Metabolic Networks were used.

## QUANTIFICATION AND STATISTICAL ANALYSIS

To assess significant differences, GraphPad 8.0 (Prism) was used. For two groups, two-tailed Student's t test was used. For more than two groups, multiple t tests were applied with Holm-Sidak correction. Two-waxy ANOVA was used to compare two variables between groups. Mantel-Cox was applied to test the incidence or survival distributions of two groups. Prior to analyzing the statistical significance of differences among treatments, we tested whether the data were normally distributed and whether variance was similar among treatments using D'Agostino and F-test, respectively. The statistical parameters can be found in the figures and the figure legends. $P \leq 0.05$ was considered significant (*), $p \leq 0.01$ (**), $p \leq 0.001$ (***).

**Cell Metabolism, Volume *33***

## Supplemental information

# Cold exposure protects from neuroinflammation through immunologic reprogramming

**Martina Spiljar, Karin Steinbach, Dorothée Rigo, Nicolas Suárez-Zamorano, Ingrid Wagner, Noushin Hadadi, Ilena Vincenti, Nicolas Page, Bogna Klimek, Mary-Aude Rochat, Mario Kreutzfeldt, Claire Chevalier, Ozren Stojanović, Olivia Bejuy, Didier Colin, Matthias Mack, Dilay Cansever, Melanie Greter, Doron Merkler, and Mirko Trajkovski**

# Figure S1

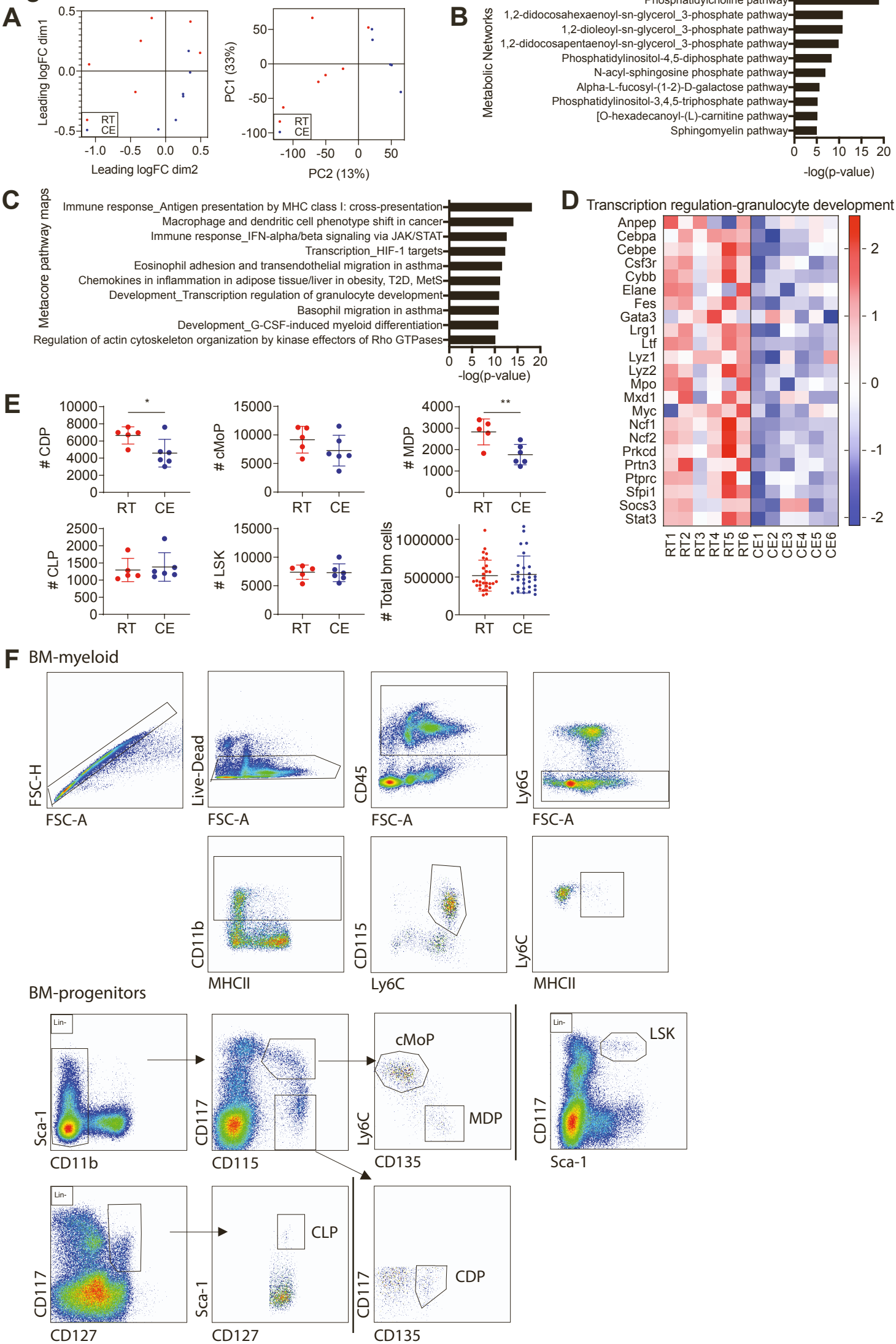
A
Leading logFC dim1
Leading logFC dim2
RT
CE
PC1 (33%)
PC2 (13%)
B
Metabolic Networks
Phosphatidylcholine pathway
1,2-didocosahexaenoyl-sn-glycerol_3-phosphate pathway
1,2-dioleoyl-sn-glycerol_3-phosphate pathway
1,2-didocosapentaenoyl-sn-glycerol_3-phosphate pathway
Phosphatidylinositol-4,5-diphosphate pathway
N-acyl-sphingosine phosphate pathway
Alpha-L-fucosyl-(1-2)-D-galactose pathway
Phosphatidylinositol-3,4,5-triphosphate pathway
[O-hexadecanoyl-(L)-carnitine pathway
Sphingomyelin pathway
-log(p-value)
C
Metacore pathway maps
Immune response_Antigen presentation by MHC class I: cross-presentation
Macrophage and dendritic cell phenotype shift in cancer
Immune response_IFN-alpha/beta signaling via JAK/STAT
Transcription_HIF-1 targets
Eosinophil adhesion and transendothelial migration in asthma
Chemokines in inflammation in adipose tissue/liver in obesity, T2D, MetS
Development_Transcription regulation of granulocyte development
Basophil migration in asthma
Development_G-CSF-induced myeloid differentiation
Regulation of actin cytoskeleton organization by kinase effectors of Rho GTPases
-log(p-value)
D
Transcription regulation-granulocyte development
Anpep
Cebpa
Cebpe
Csf3r
Cybb
Elane
Fes
Gata3
Lrg1
Ltf
Lyz1
Lyz2
Mpo
Mxd1
Myc
Ncf1
Ncf2
Prkcd
Prtn3
Ptprc
Sfpi1
Socs3
Stat3
RT1 RT2 RT3 RT4 RT5 RT6 CE1 CE2 CE3 CE4 CE5 CE6
E
# CDP
# cMoP
# MDP
# CLP
# LSK
# Total bm cells
RT
CE
F
BM-myeloid
FSC-H
FSC-A
Live-Dead
CD45
Ly6G
CD11b
MHCII
CD115
Ly6C
BM-progenitors
Lin-
Sca-1
CD117
cMoP
MDP
LSK
CD135
CD127
CLP
CDP

**Figure S1. Cold housing temperature causes immunological alterations, Related to Figure 1**

(A) Multidimensional scaling and principal component analysis of the bone marrow from mice after 2 weeks of cold exposure at 10°C compared to room temperature mice.

(B) 10 most enriched Metacore Metabolic Networks of mice as in (A).

(C) Metacore Pathway Maps analysis identifying the 10 most differentially regulated pathways of mice as in (A).

(D) 1 of 4 heatmaps that were consistently changed (> 80% of genes in the same direction) from the top 10 deregulated Metacore Pathway Maps of mice as in (A).

(E) Absolute cell numbers within the bone marrow of mice as in Figure 1F as determined by flow cytometry. Shown is one experiment or for total bone marrow cells a pool of 5 experiments, mean ±SD and significance was calculated using student's t test, * $p<0.05$, ** $p<0.01$.

(F) Bone marrow monocytes were gated as live, single, $CD45^+$, $Ly6G^-$, $CD11b^+$, $CD115^+$, $Ly6C^+$ cells and $MHCII^+$ population determined. Bone marrow progenitors were all gated as single, live, CD45+, Lin- (NK1.1, CD3, CD19, Ter119, Ly6G) and $CD11b^-$, $Sca1^+$, $CD117^{hi}$, $CD115^+$, $Ly6C^{hi}$ (cMoP), $CD11b^-$, $Sca1^+$, $CD117^{hi}$, $CD115^+$, $Ly6C^-$ (MDP), $CD11b^-$, $Sca1^+$, $CD117^-$, $CD115^+$, $CD135^+$ (MDP), $CD117^+$, CD127+, $Sca\text{-}1^+$ (CLP), $Sca\text{-}1^+$, $CD117^+$ (LSK).

(C-D) The cutoff on differentially regulated genes considered for the pathway analysis is $p<0.05$ and pathways are considered deregulated with $p<0.05$. Shown are –log(p-value).

# Figure S2

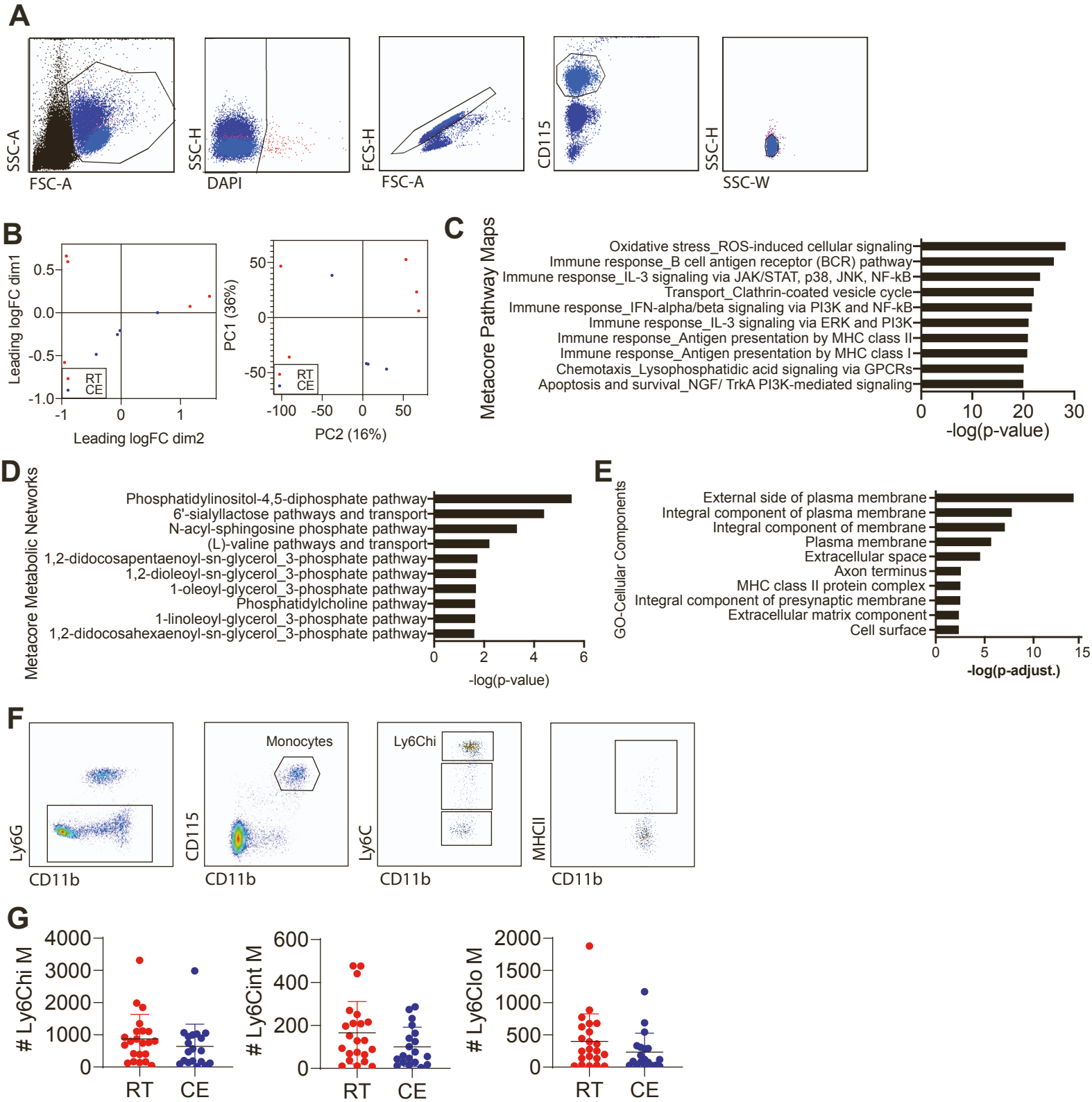
A
SSC-A
FSC-A
SSC-H
DAPI
FCS-H
FSC-A
CD115
SSC-H
SSC-W
B
Leading logFC dim1
Leading logFC dim2
RT
CE
PC1 (36%)
PC2 (16%)
C
Metacore Pathway Maps
Oxidative stress_ROS-induced cellular signaling
Immune response_B cell antigen receptor (BCR) pathway
Immune response_IL-3 signaling via JAK/STAT, p38, JNK, NF-kB
Transport_Clathrin-coated vesicle cycle
Immune response_IFN-alpha/beta signaling via PI3K and NF-kB
Immune response_IL-3 signaling via ERK and PI3K
Immune response_Antigen presentation by MHC class II
Immune response_Antigen presentation by MHC class I
Chemotaxis_Lysophosphatidic acid signaling via GPCRs
Apoptosis and survival_NGF/ TrkA PI3K-mediated signaling
-log(p-value)
D
Metacore Metabolic Networks
Phosphatidylinositol-4,5-diphosphate pathway
6'-sialyllactose pathways and transport
N-acyl-sphingosine phosphate pathway
(L)-valine pathways and transport
1,2-didocosapentaenoyl-sn-glycerol_3-phosphate pathway
1,2-dioleoyl-sn-glycerol_3-phosphate pathway
1-oleoyl-glycerol_3-phosphate pathway
Phosphatidylcholine pathway
1-linoleoyl-glycerol_3-phosphate pathway
1,2-didocosahexaenoyl-sn-glycerol_3-phosphate pathway
-log(p-value)
E
GO-Cellular Components
External side of plasma membrane
Integral component of plasma membrane
Integral component of membrane
Plasma membrane
Extracellular space
Axon terminus
MHC class II protein complex
Integral component of presynaptic membrane
Extracellular matrix component
Cell surface
-log(p-adjust.)
F
Ly6G
CD11b
Monocytes
CD115
CD11b
Ly6Chi
Ly6C
CD11b
MHCII
CD11b
G
# Ly6Chi M
# Ly6Cint M
# Ly6Clo M
RT
CE

**Figure S2. Cold modulates blood monocytes, Related to Figure 2**

(A) Gating strategy for the FACS (CD115-PE+) sort after MACS (anti-PE) sort before RNA sequencing from blood of 2 weeks cold exposed (10°C) compared to room temperature mice. Sorted were DAPI-, single, CD115+ cells.

(B) Multidimensional scaling (left) and principal component analysis (right) after RNA sequencing of monocytes as in (A).

(C-E) 10 most differentially regulated Metacore Pathway Maps without p-value cutoff on considered genes (C), Metacore Metabolic Networks (D) and Gene Ontology Cellular Components (E). Genes were considered as differentially regulated genes with $p<0.05$ and pathways are considered deregulated or enriched with $p<0.05$. Shown are –log(p-value).

(F) For flow cytometry analysis, blood monocytes were gated as $Ly6G^-$, $CD11b^+$, $CD115^+$, $Ly6C^{hi/int/lo}$ and $MHCII^+$ positive population was gated.

(G) Absolute cell numbers within the blood of mice as in Figure 2D as determined by flow cytometry. Shown is a pool of three experiments and mean ±SD.

# Figure S3

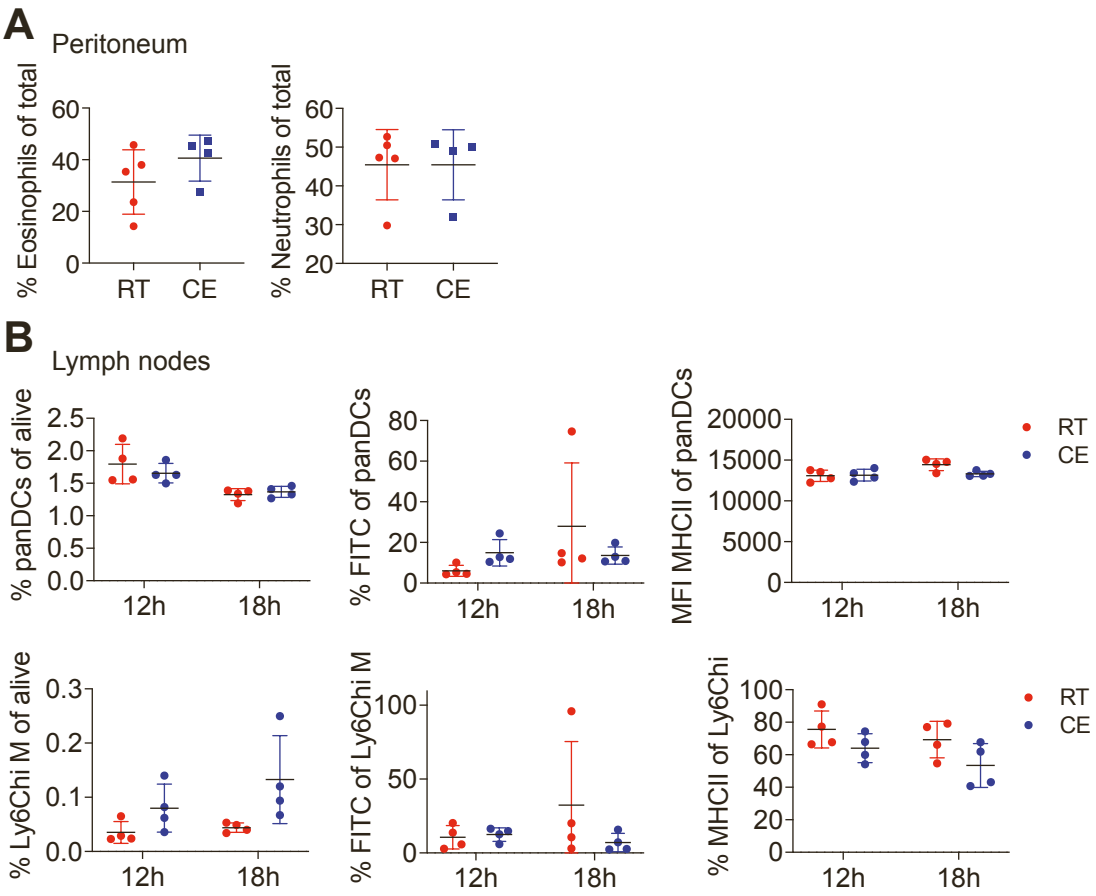
A
Peritoneum
% Eosinophils of total
60
40
20
0
RT
CE
% Neutrophils of total
60
50
40
30
20
RT
CE
B
Lymph nodes
% panDCs of alive
2.5
2.0
1.5
1.0
0.5
0.0
12h
18h
% FITC of panDCs
80
60
40
20
0
12h
18h
MFI MHCII of panDCs
20000
15000
10000
5000
0
12h
18h
RT
CE
% Ly6Chi M of alive
0.3
0.2
0.1
0.0
12h
18h
% FITC of Ly6Chi M
100
50
0
12h
18h
% MHCII of Ly6Chi
100
80
60
40
20
0
12h
18h
RT
CE

**Figure S3. Cold reduces monocyte MHCII, Related to Figure 3**

(A) Peritoneal fluid cells were analyzed by flow cytometry 24h after i.p. injection with thioglycollate into two weeks cold exposed (10°C) or room temperature mice. Shown is mean ±SD.

(B) Flow cytometry analysis of lymph node draining cells 12 and 18 hours after FITC skin painting on one flank of 2 weeks cold exposed (10°C) or room temperature mice. Percentage of panDCs (upper) and Ly6C$^{hi}$ monocytes (bottom), their FITC uptake and MHCII expression. Shown is mean ±SD, two-way ANOVA. Every dot represents one animal and the experiment is representative of two.

# Figure S4

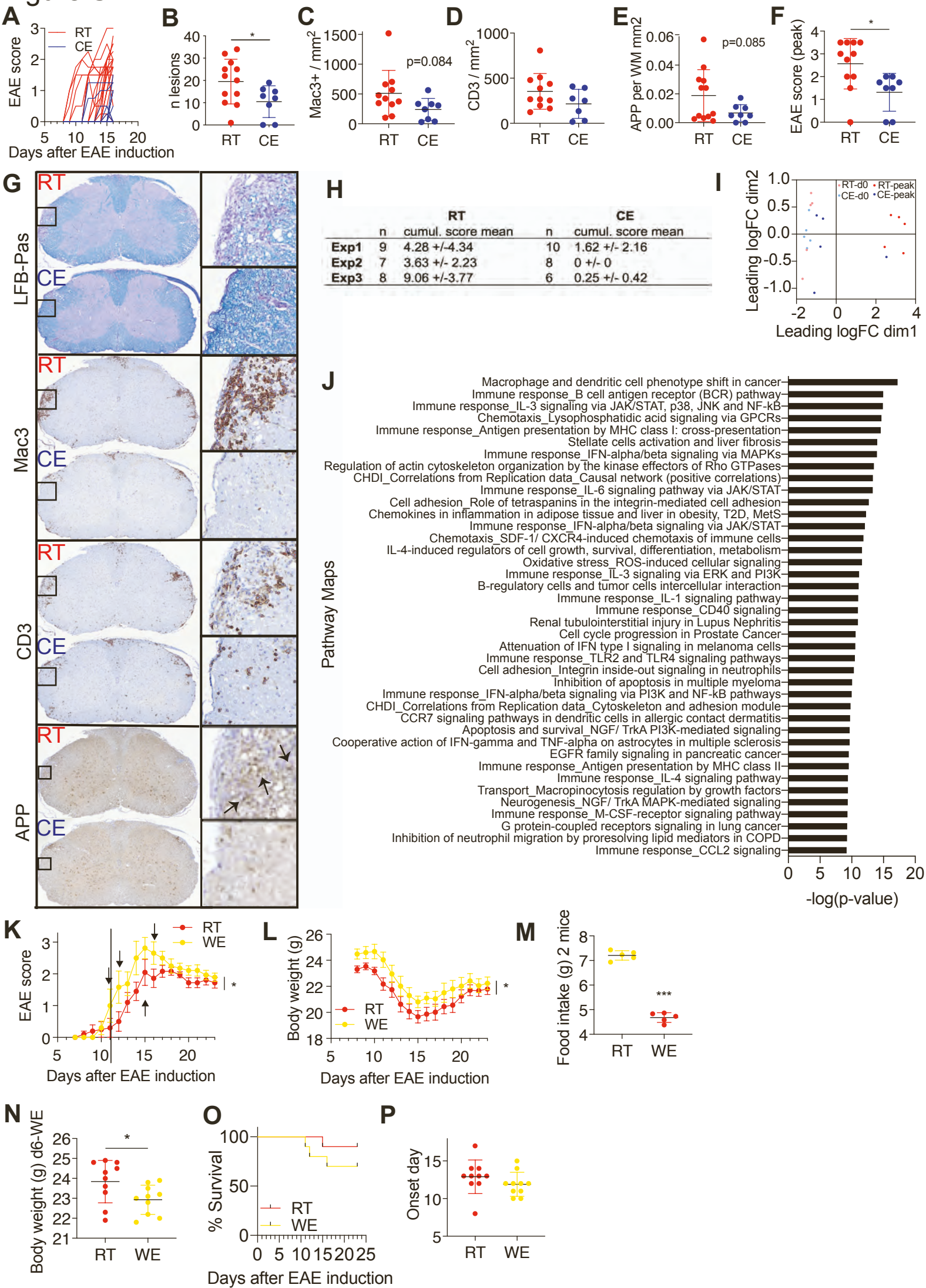
A
EAE score
RT
CE
Days after EAE induction
B
n lesions
RT
CE
C
Mac3+ / mm2
p=0.084
D
CD3 / mm2
E
APP per WM mm2
p=0.085
F
EAE score (peak)
G
RT
CE
LFB-Pas
Mac3
CD3
APP
H
RT
CE
n
cumul. score mean
Exp1 9 4.28 +/-4.34 10 1.62 +/- 2.16
Exp2 7 3.63 +/- 2.23 8 0 +/- 0
Exp3 8 9.06 +/-3.77 6 0.25 +/- 0.42
I
RT-d0
RT-peak
CE-d0
CE-peak
Leading logFC dim2
Leading logFC dim1
J
Pathway Maps
Macrophage and dendritic cell phenotype shift in cancer
Immune response_B cell antigen receptor (BCR) pathway
Immune response_IL-3 signaling via JAK/STAT, p38, JNK and NF-kB
Chemotaxis_Lysophosphatidic acid signaling via GPCRs
Immune response_Antigen presentation by MHC class I: cross-presentation
Stellate cells activation and liver fibrosis
Immune response_IFN-alpha/beta signaling via MAPKs
Regulation of actin cytoskeleton organization by the kinase effectors of Rho GTPases
CHDI_Correlations from Replication data_Causal network (positive correlations)
Immune response_IL-6 signaling pathway via JAK/STAT
Cell adhesion_Role of tetraspanins in the integrin-mediated cell adhesion
Chemokines in inflammation in adipose tissue and liver in obesity, T2D, MetS
Immune response_IFN-alpha/beta signaling via JAK/STAT
Chemotaxis_SDF-1/ CXCR4-induced chemotaxis of immune cells
IL-4-induced regulators of cell growth, survival, differentiation, metabolism
Oxidative stress_ROS-induced cellular signaling
Immune response_IL-3 signaling via ERK and PI3K
B-regulatory cells and tumor cells intercellular interaction
Immune response_IL-1 signaling pathway
Immune response_CD40 signaling
Renal tubulointerstitial injury in Lupus Nephritis
Cell cycle progression in Prostate Cancer
Attenuation of IFN type I signaling in melanoma cells
Immune response_TLR2 and TLR4 signaling pathways
Cell adhesion_Integrin inside-out signaling in neutrophils
Inhibition of apoptosis in multiple myeloma
Immune response_IFN-alpha/beta signaling via PI3K and NF-kB pathways
CHDI_Correlations from Replication data_Cytoskeleton and adhesion module
CCR7 signaling pathways in dendritic cells in allergic contact dermatitis
Apoptosis and survival_NGF/ TrkA PI3K-mediated signaling
Cooperative action of IFN-gamma and TNF-alpha on astrocytes in multiple sclerosis
EGFR family signaling in pancreatic cancer
Immune response_Antigen presentation by MHC class II
Immune response_IL-4 signaling pathway
Transport_Macropinocytosis regulation by growth factors
Neurogenesis_NGF/ TrkA MAPK-mediated signaling
Immune response_M-CSF-receptor signaling pathway
G protein-coupled receptors signaling in lung cancer
Inhibition of neutrophil migration by proresolving lipid mediators in COPD
Immune response_CCL2 signaling
-log(p-value)
K
EAE score
RT
WE
Days after EAE induction
L
Body weight (g)
Days after EAE induction
M
Food intake (g) 2 mice
N
Body weight (g) d6-WE
O
% Survival
Days after EAE induction
P
Onset day

**Figure S4. Cold alleviates, while warm worsens neuroinflammation, Related to Figure 4**

(A) Individual EAE curve (as in Figure 4A) of each room temperature and cold-exposed mouse.

(B-G) Histology on sagittal spinal cord sections of cold-exposed and room temperature peak EAE mice. Number of lesions that were found in both LFB-PAS and APP staining were quantified in APP staining (B). Immunohistochemistry using anti-mac3 (C) and anti-CD3 antibody (D). APP staining was quantified within areas identified as demyelinated in LFB-PAS staining and presented as percentage per white matter area (E). EAE disease score at sacrifice of mice in which histology was performed (F). LFB-PAS stain shows demyelinated areas within the white matter in purple (first panel), anti-mac3 stains mac3+ macrophages (second panel), anti-CD3 stains T cells in brown (third panel) and amyloid precursor protein (APP) accumulates at axons with impaired axonal transport, a surrogate for acute axonal damage (fourth panel). Arrows identify punctuated APP-positive axonal spheroids. (G). Anti-mac3, anti-CD3 and anti-APP stainings were developed with DAB and nuclei counterstained with hemalum.

(H) Table of cumulative EAE scores ±SD and number of mice of each individual experiment.

(I, J) Multidimensional scaling analysis of spinal cord from mice as in Figure 4J (I). Top 35 Metacore Metabolic Network pathways of mice with EAE, genes with $p<0.05$ were included for analysis (J).

(K-P) EAE disease curve of warm exposed (34°C, started one week before immunization) or room temperature mice. Arrows indicate individual mice that died or had to be sacrificed, which received a score of five on the day of death (K). Body weight during the course of EAE (L). Food intake of two mice per cage within 24 h on

day 6 of warm exposure (M) and body weight on day six of warm exposure (N), before immunization. Survival of mice during EAE (O) and day of EAE onset (P).

(B-F, K-P) Shown is mean ±SEM, two-way ANOVA (K, L); Mantel-Cox (O), student's t test (B-F, L-M, P) with mean ±SD, $^{*}p < 0.05$, $^{**}p < 0.01$, $^{***}p < 0.001$.

Figure S5

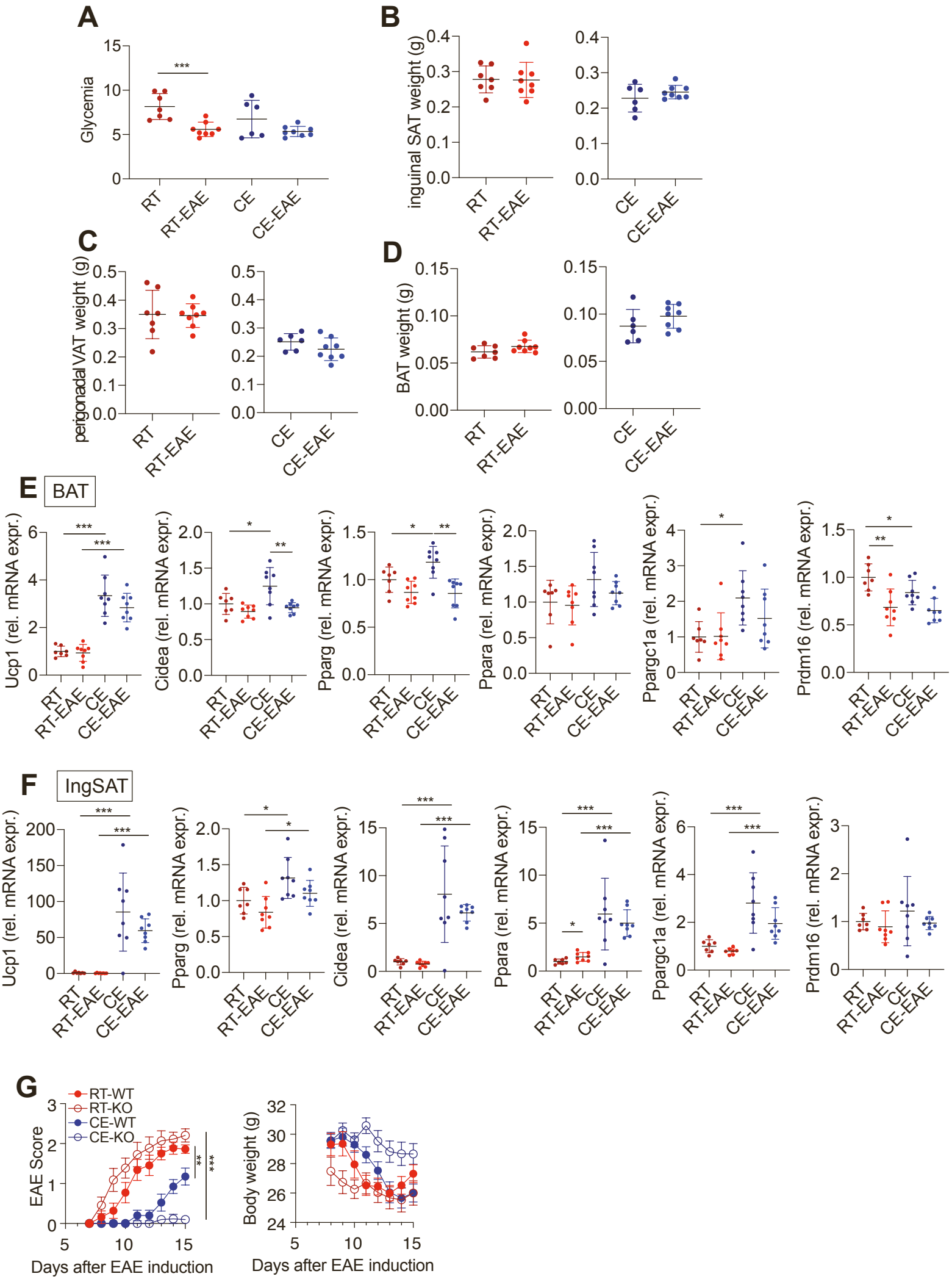
A
Glycemia
B
inguinal SAT weight (g)
C
perigonadal VAT weight (g)
D
BAT weight (g)
RT
RT-EAE
CE
CE-EAE
E
BAT
Ucp1 (rel. mRNA expr.)
Cidea (rel. mRNA expr.)
Pparg (rel. mRNA expr.)
Ppara (rel. mRNA expr.)
Ppargc1a (rel. mRNA expr.)
Prdm16 (rel. mRNA expr.)
F
IngSAT
G
RT-WT
RT-KO
CE-WT
CE-KO
EAE Score
Days after EAE induction
Body weight (g)
Days after EAE induction

**Figure S5. Metabolic profiling of cold-exposed mice after immunisation, Related to Figure 5**

(A) Glycemia on day 8 of EAE after 3 hours of fasting. Mice were cold exposed for 2 weeks before immunisation and during EAE or steady state. Control mice were at room temperature for the same duration.

(B-D) Adipose tissue weights of inguinal subcutaneous adipose tissue (B), perigonadal visceral adipose tissue (C) o, or interscapular brown (D) of mice as in (A).

(E-F) mRNA expression of browning markers relative to *B2m* and *36b4* in interscapular brown (E) and inguinal subcutaneous adipose tissue (F) of mice as in (A) as determined by qPCR.

(G) Symptoms of EAE (left) and body weight (right) in *Ucp1*-knockout (KO) and their respective wildtype (WT) littermate controls housed at room temperature or cold for 1 week before and during EAE. Shown is 1 representative (n=10-15 per group) of 2 experiments.

(A-G, I) Multiple t-test with Holm-Sidak correction (A,E,F), students t-test (B-D), two-way ANOVA (G). (A-F) show mean ±SD; (G) shows mean ±SEM. $*p < 0.05$, $**p < 0.01$, $***p < 0.001$.

# Figure S6

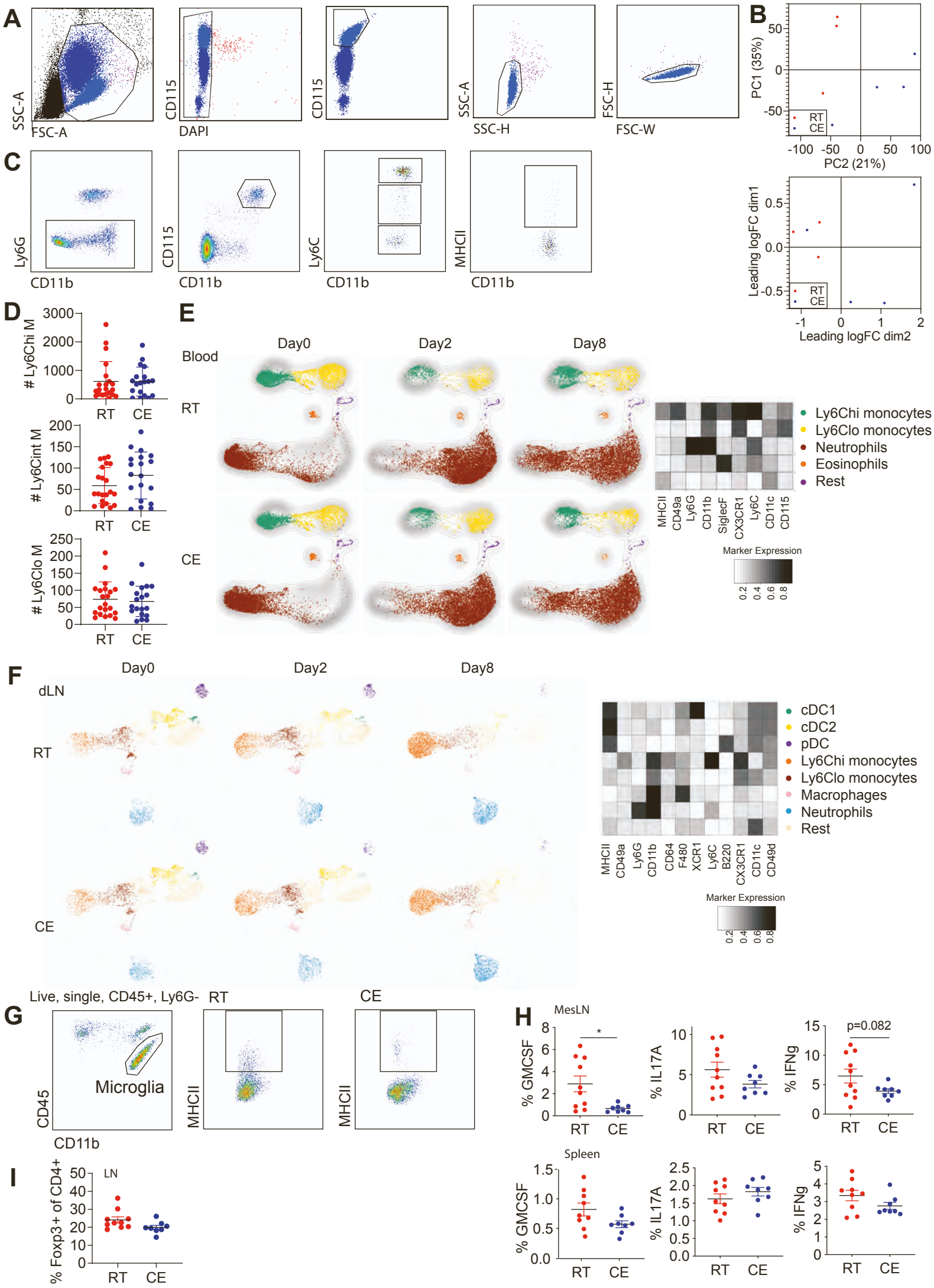
A
SSC-A
FSC-A
CD115
DAPI
CD115
SSC-A
SSC-H
FSC-H
FSC-W
B
PC1 (35%)
PC2 (21%)
RT
CE
Leading logFC dim1
Leading logFC dim2
C
Ly6G
CD11b
CD115
CD11b
Ly6C
CD11b
MHCII
CD11b
D
# Ly6Chi M
# Ly6Cint M
# Ly6Clo M
RT
CE
E
Blood
Day0
Day2
Day8
RT
CE
MHCII
CD49a
Ly6G
CD11b
SiglecF
CX3CR1
Ly6C
CD11c
CD115
Marker Expression
Ly6Chi monocytes
Ly6Clo monocytes
Neutrophils
Eosinophils
Rest
F
dLN
Day0
Day2
Day8
RT
CE
MHCII
CD49a
Ly6G
CD11b
CD64
F480
XCR1
Ly6C
B220
CX3CR1
CD11c
CD49d
Marker Expression
cDC1
cDC2
pDC
Ly6Chi monocytes
Ly6Clo monocytes
Macrophages
Neutrophils
Rest
G
Live, single, CD45+, Ly6G-
RT
CE
CD45
Microglia
CD11b
MHCII
MHCII
H
MesLN
% GMCSF
% IL17A
% IFNg
p=0.082
Spleen
% GMCSF
% IL17A
% IFNg
I
LN
% Foxp3+ of CD4+
RT
CE

**Figure S6. Cold reduces monocyte and T cell pathogenicity during neuroinflammation, Related to Figure 6**

(A) Gating strategy for the FACS sort after MACS sorting before RNA sequencing (as in Figure 6A). Sorted were DAPI-, $CD115^+$, single cells.

(B) Multidimensional scaling and principal component analysis of FACS sorted blood monocytes at EAE onset as in Figure 6A.

(C) Gating strategy for MHCII expression on $Ly6C^{hi}$ blood monocytes of mice as in Figure 6A. Cells were gated as single, $Ly6G^-$, $CD115^+CD11b^+$, $Ly6C^{hi}$, $MHCII^+$.

(D) Absolute cell numbers within the blood of mice as in Figure 5D as determined by flow cytometry. Shown is a pool of three experiments and mean ±SD. Pool of 3 experiments. (E-F) Blood (E) and lymph node (F) immune cells of mice as in Figure 6A on different days after immunization were visualized using UMAP and clustered using the FlowSOM algorithm in R. Heatmap shows median relative expression of all panel markers.

(G) Gating strategy for MHCII expression on microglia of mice as in Figure 6A. Cells were gated as single, live, $Ly6G^-$, CD45int, $MHCII^+$.

(H) Flow cytometry analysis of mesenteric LN (upper panel) or spleen cells (lower panel) of mice as in Figure 6A at EAE onset. Percentage of cytokine expression in $CD4^+$ T cells. Shown is mean ±SD, significance was calculated using student's t test, * $p<0.05$.

(I) Flow cytometry analysis of draining LN of mice as in Figure 6A at EAE onset. Percentage of Foxp3+ Tregs of total $CD4^+$ T cells. Shown is mean ±SD.

Figure S7

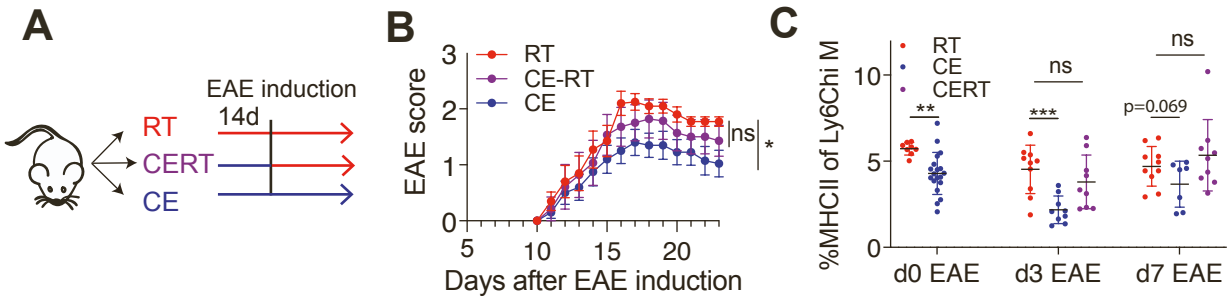
A
EAE induction
14d
RT
CERT
CE
B
EAE score
RT
CE-RT
CE
ns
*
Days after EAE induction
C
%MHCII of Ly6Chi M
RT
CE
CERT
**
ns
***
ns
p=0.069
d0 EAE
d3 EAE
d7 EAE

**Figure S7. Transferring cold-exposed mice to room temperature prior to T cell priming limits the beneficial cold-induced effects, Related to Figure 7**

(A-B) Scheme showing experimental setup for cold exposure and EAE (A). Cold exposure either started two weeks before and continued during EAE (blue, CE) or switched to room temperature from the day of immunization (violet, CE-RT) and compared to room temperature mice (red, B). EAE disease curve shown as mean ±SEM, two-way ANOVA, $^{*}p < 0.05$.

(C) Percentage of MHCII expression of $Ly6C^{hi}$ blood monocytes via flow cytometry on day zero, day three and day seven after EAE induction. Multiple t-test with Holm-Sidak correction with mean ±SD, $^{*}p < 0.05$, $^{**}p < 0.01$, $^{***}p < 0.001$.